Size-effect in Very High Cycle Fatigue: A review

Size-effect in Very High Cycle Fatigue: a review

Authors:
A. Tridello[a], C. Boursier Niutta[b], F. Berto[c], D.S. Paolino[d]

[a] Department of Mechanical and Aerospace Engineering, Politecnico di Torino, 10129 Turin, Italy, andrea.tridello@polito.it
[b] Department of Mechanical and Aerospace Engineering, Politecnico di Torino, 10129 Turin, Italy, carlo.boursier@polito.it
[c] Department of Mechanical and Industrial Engineering, Norwegian University of Science and Technology (NTNU), Richard Birkelands vei 2b, 7491 Trondheim, Norway, filippo.berto@ntnu.no
[d] Department of Mechanical and Aerospace Engineering, Politecnico di Torino, 10129 Turin, Italy, davide.paolino@polito.it

Corresponding Author:
A. Tridello
E-mail address: andrea.tridello@polito.it
Full postal address:
C.so Duca degli Abruzzi 24,
Department of Mechanical and Aerospace Engineering – Politecnico di Torino,
10129 – Turin,
ITALY
Phone number: +39.011.090.6913
Fax number: +39.011.090.6999

Abstract

It is well-known that fatigue failures in VHCF originate from defects present within the risk-volume. Moreover, experimental results have shown that the larger the specimen size and the risk-volume, the shorter is the VHCF life. This is known as *size-effect* and is generally due to the statistical increment of the defect size with the material volume.

In the paper, size-effect in VHCF is critically revised. The experimental results obtained by testing specimens with different sizes are analyzed and the methodologies proposed to model size-effect are discussed, with the aim of guiding the future research on size-effect in VHCF.

Keywords: Very-High-Cycle Fatigue (VHCF); size-effect; risk-volume; Largest Extreme Value Distribution (LEVD); fatigue limit.

Nomenclature

$a_{d,0}$: area of the initial defect size.

a_{ODA}: size of the ODA surrounding the initial defect.

K_{th}: SIF threshold.

N_f: number of cycles to failure.

P-S-N curve: Probabilistic S-N curve.

rv: random variable.

SIF: Stress Intensity Factor.

s_a: stress amplitude.

s_l: fatigue limit.

VHCF: Very High Cycle Fatigue.

1. INTRODUCTION

The component design against static and fatigue failures is based on mechanical properties that are generally assessed through laboratory experimental tests on small specimens, with sizes that differ significantly from those of the final components. However, mechanical properties of materials can vary depending on the part size, like the diameter or the volume. This phenomenon is called size or scale effect [1-6]. For example, it is well-known that the High Cycle Fatigue (HCF) strength decreases with the specimen diameter [7]: the larger the diameter, the smaller the HCF strength. This dependency must be carefully accounted when components are designed, in order to guarantee their structural integrity [7-9].

Size-effect has also a significant influence on the Very High Cycle Fatigue (VHCF) response of materials. In this fatigue life range, i.e., beyond 10^8 cycles, it is well-known that the crack mainly originates from internal defects with mechanisms that are different from those occurring in HCF. Moreover, the fracture surface generally shows a peculiar morphology, with a characteristic region surrounding the initial defect [10], which is called Optically Dark Area (ODA [11]), Fine Granular Area (FGA [12, 13]), Granular Bright Facet, (GBF [14]), depending on the measuring technique. Size-effect in VHCF is generally analysed by considering the statistical distribution of the defects originating the fatigue failures within the highly stressed volume, which is generally referred to as "risk-volume". According to [8], the larger the risk-volume, the larger the probability of large defects, with a consequent decrement of the VHCF response. Therefore, the defect size and the risk-volume strongly affect the VHCF response of materials. More recently, a different theoretical explanation has been provided for size-effect in VHCF, based on lacunar fractality concepts [15, 16]. These experimental investigations point out that size-effect in VHCF is debated in the literature and a unique theory or model is not available.

The main issue concerning the experimental assessment of size-effect in VHCF is the complexity of testing full-scale components to validate the models developed in the literature. Indeed, tests for assessing the VHCF of materials are time-consuming and are in the majority of the cases carried out with ultrasonic fatigue testing machines [17, 18] working in resonance conditions and on specimens designed in order to have the first longitudinal resonance frequency close to $20\ \mathrm{kHz}$. Accordingly, tests on full-scale components cannot be carried out with this technique. On the other hand, tests at conventional frequencies (less than $50\ \mathrm{Hz}$) may be carried out on full-scale components, but with too high testing time (e.g., at $20\ \mathrm{kHz}$, 10^9 cycles are tested in more than 5 months). The only strategy is therefore to enlarge the size of the specimens tested through ultrasonic tests, but, even in this case, the specimen volume is significantly smaller than that of real components. For this reason, the assessment of size-effect in VHCF is complex and the models developed in the literature can be hardly validated through tests on real components.

In the present paper, the experimental results and the models available in the literature for analysing size-effect in VHCF are reviewed. At first, the importance of properly defining the "risk-volume" is discussed. The second part focuses on the influence of the risk-volume and of the defect size on size-effect in VHCF.

Thereafter, the influence of the specimen diameter on size-effect is discussed. Finally, the design procedures that take into account size-effect in VHCF are described and results available in the literature are discussed, to try to find some general rules concerning size-effect in VHCF and to guide future research.

2. SIZE-EFFECT IN VHCF

In this Section, the experimental results on size-effect in VHCF and the models available in the literature on its influence are analyzed. In Section 2.1, important concepts regarding the Largest Extreme Value Distribution (LEVD) that is commonly used for dealing with size-effect in VHCF are recalled. In Section 2.2, the definitions for the risk-volume available in the literature are discussed. The influence of size-effect on the fatigue limit and on the fatigue life is investigated in Section 2.3 and Section 2.4, respectively. Finally, in Section 2.5, the papers that investigate size-effect in VHCF by considering the specimen diameter or the specimen size as the most influencing parameters, rather than the specimen volume, are analyzed.

For the sake of clarity, with risk-volume, V_{risk}, the authors generically refer to the volume at risk of crack nucleation. If the risk-volume is defined by considering a specific x threshold stress ratio percentage, the risk-volume will be called V_x: for example, with V_{90} the authors refer to the volume of material above the 90% of the largest applied stress. Moreover, for the peculiar area around the defect, i.e., the Optically Dark Area (ODA) or the Fine Granular Area (FGA) [10], the name used in the original paper is maintained in the present paper to avoid confusion. Finally, "Authors" (with the upper-case initial letter) refer to the authors of the original paper, whereas authors (with the lower-case initial letter) refer to the authors of the present paper. N_f, s_a, SIF, s_l, HV are the number of cycles to failure, the applied stress amplitude, the Stress Intensity Factor, the fatigue limit and the Vickers hardness, respectively. "Gage section" refer to the minimum cross-section for the hourglass and the dog-bone specimens. For the Gaussian specimens [19], the gage diameter is the diameter at the beginning of the part with profile described by a Gaussian function.

2.1. Largest Extreme Valued Distribution (LEVD) for the defect size

It is well-known that the mechanisms of crack initiation in VHCF are different from those in the LCF-HCF life range. Indeed, the crack generally originates from the specimen surface in the LCF-HCF life range, whereas it forms from defects randomly distributed within the risk-volume in VHCF. Moreover, the peculiarity of the VHCF failures is that the crack can form from an initial defect characterized by a SIF smaller than the SIF threshold. The defect population, therefore, controls the VHCF response. In particular, according to [8], the larger the defect, the smaller the VHCF strength, with the defect size being the most influencing factor, rather than the defect shape or its chemical composition. An analysis of the VHCF response must, therefore, take into account the defect size and its random distribution.

Defects in the material volume have different three-dimensional shapes and morphologies [8, 20], but, according to [8], their influence can be assessed by considering the geometrical parameter $\sqrt{area}$, i.e., the

square root of the area of the defect obtained by projecting it in a plane perpendicular to the maximum tensile stress. The characteristic defect size, $\sqrt{area}$ ($\sqrt{a_{d,0}}$ in the following) is a random variable and is assumed to follow a Largest Extreme Distribution, LEVD, with cumulative distribution function (cdf) $F_{\sqrt{a_{d,0}}}\left(\sqrt{a_{d,0}}\right)$ given by:

$$F_{\sqrt{a_{d,0}}}\left(\sqrt{a_{d,0}}\right) = e^{-e^{-\left(\frac{\sqrt{a_{d,0}}-\mu_{\sqrt{a_{d,0}}}}{\sigma_{\sqrt{a_{d,0}}}}\right)}}, \quad (1)$$

where $\mu_{\sqrt{a_{d,0}}}$ and $\sigma_{\sqrt{a_{d,0}}}$ are the location and the scale parameter of the LEVD. Equation 1 enables to compute the probability of having a defect with size smaller than $\sqrt{a_{d,0}}$ in the investigated material volume V_0. By exploiting the LEVD properties, the cdf of the LEVD for the same material (i.e., with the same coefficients $\mu_{\sqrt{a_{d,0}}}$ and $\sigma_{\sqrt{a_{d,0}}}$) but for a material volume V_n, n times larger than V_0 (i.e., $V_n = n \cdot V_0$), can be obtained by Eq. 2:

$$F_{\sqrt{a_{d,0}}}\left(\sqrt{a_{d,0}}\right) = e^{-e^{-\left(\frac{\sqrt{a_{d,0}}-\mu_{n,\sqrt{a_{d,0}}}}{\sigma_{\sqrt{a_{d,0}}}}\right)}}, \quad (2)$$

where $\mu_{n,\sqrt{a_{d,0}}} = \mu_{\sqrt{a_{d,0}}} + ln(n) \cdot \sigma_{\sqrt{a_{d,0}}}$. With easy passages, the α-th quantile of the defect size in a volume V_n can be obtained according to Eq. 3:

$$\sqrt{a}_n = \mu_{\sqrt{a}} + \sigma_{\sqrt{a}} \cdot (-ln(-ln(\alpha)) + ln(n)), \quad (3)$$

The LEVD enables therefore to model the dependency between the defect size and the material volume. It is worth noting that not only the defect size, but also the ODA size must be considered when the VHCF response is analyzed, according to [8]. However, the ODA size and the defect size can be correlated [21, 22], and a proper assessment of size-effect must consider both the defect size and the ODA size. Other important terms in Eqs. 2-3 are the volumes V_n and V_0, i.e., the volumes of material that must be considered for the application of the LEVD, corresponding to the specimen or the component risk-volume. For applied loads inducing a uniform stress distribution in the material volume under test, the risk-volume is uniquely defined as the region of material subjected to the maximum applied stress. On the other hand, if the stress distribution is not uniform within the volume under test, e.g., in case of bending loads or in ultrasonic fatigue tests [17, 23], the volume at risk of crack nucleation should be properly defined in order to safely adopt Eqs. 2 and 3. In the following Section, the approaches available in the literature for defining the risk-volume are reviewed and discussed.

2.2. Risk-volume definition

The proper choice of the volume at risk, i.e., the volume characterized by a high risk of crack nucleation if a defect is present, is of fundamental importance for the assessment of size-effect in VHCF. Its definition is still debated in the literature, in particular for loads involving a non-uniform stress distribution within the specimen or the component volume, since in this case randomly distributed defects are subjected to different applied stresses. Accordingly, the largest defect may not be the most critical defect, i.e., the one from which the crack can originate. For this reason, the defect initiating the fatigue crack will be called "critical defect". As pointed out in Section 2.1, if the stress amplitude is constant within the material volume, the risk-volume is clearly the volume of material subjected to the maximum applied stress and the largest defect will correspond to the critical defect. However, this situation is not common in practical applications. Generally, experimental VHCF tests are carried out with rotating bending testing machines [24], or, dominantly, by using the ultrasonic testing machines. In the latter case, the specimens work in resonance conditions, with a loading frequency in the range $[19 - 21]\ kHz$. The distribution of the stress amplitude within the material is not constant, even within the straight section of dog-bone specimens [23, 25]. A variable stress amplitude within the material volume is, moreover, a common condition in real-world components and particular attention must be posed on the choice of the volume at risk, as it could influence the results. For example, the choice of the whole component volume as the risk-volume can be too conservative, since very large defects in less stressed regions are not critical. On the other hand, a portion of the total volume can be considered as the risk-volume, but the criterion for this subdivision should be properly chosen and validated.

In [8], the risk-volume is assumed as the "volume of material subjected to a stress amplitude larger than the 90% of the maximum applied stress" (V_{90}). This definition is obtained by analyzing the results of a large number of rotating bending fatigue tests obtained on steel specimens by the Authors and available in the literature. The Authors found that almost all fatigue failures are concentrated in a region of material subjected to a stress amplitude larger than the 90% of the maximum applied stress. This justified the choice of the V_{90} for the region at risk. However, rare large inclusions were also found at the origin of the fatigue cracks, with $\sqrt{a_{d,0}} > 100\ \mu m$, in the region outside the V_{90}. The Authors pointed out that these very large inclusions were found in steels tested in the past (in the 1963) and that in more recent steels these very large inclusions are not present. The Authors also pointed out that, even if a large percentage of the stress ratio threshold is considered (80% or 70%), the predicted fatigue limit is not strongly affected. This because the fatigue limit estimated with Murakami's formulation [8] conservatively refers to the nominal stress at the specimen surface, whereas the stress amplitude involved in the crack nucleation process is the local stress amplitude close to the defect. These results are obtained through rotating bending tests on round bars. For the hourglass specimens, a threshold stress ratio in the range [95% - 90%] was on the other hand suggested. It must be noted that the defects analysed in [8] are mainly found by observing the fracture surfaces of specimens subjected to HCF rotating bending tests, with the fatigue cracks originating from surface defects

or in a material region close to the surface. Indeed, in rotating bending tests, even if large defects below the 90% threshold stress ratio are present, they can be hardly at the origin of the fatigue failures, due to the high-stress gradient generated by a bending load. However, in VHCF tests internal defects play the most important role, which limits the validity of the 90% threshold volume in this fatigue regime. Moreover, even if the considerations in [8] are valid for most of the recent pure high strength steels, which rarely show inclusions larger than $100\ \mu m$, they are not valid for other materials or specific production processes, like the parts produced by Additive Manufacturing (AM) processes and characterized by very large defects [26, 27]. Accordingly, even defects located outside the V_{90} can be critical.

Murakami proposed a procedure for the estimation of the largest defect through defect sampling on limited portions of polished surface, with size S_0.The volume V_0 associated to each polished surface is computed as:

$$V_0 = h_0 \cdot S_0, \tag{4}$$

where h_0 is the average value of the defect size. This methodology avoids performing time-consuming and expensive VHCF tests. However, the defect population found on polished surfaces can be different from that originating failures in large volume, according to [8].

The approach based on the threshold stress ratio has been largely used in the literature for assessing the influence of size-effect in VHCF. For example, in [28], a 95% threshold stress was considered, but the Authors did not provide indications for this choice. On the other hand, the 90% threshold stress ratio proposed by Murakami has been considered for the analysis of the VHCF test results in almost all the cases. Indeed, this approach enables to easily compute the volume at risk and it generally works for different types of high strength steels, for which only defects in the material region subjected to a stress amplitude close to the maximum applied stress are critical. For these reasons, the V_{90} has proved to be a good compromise for the assessment of the volume at risk. For example, in [25], ultrasonic fully reversed tension-compression tests have been carried out on dog-bone and hourglass specimens with different V_{90}. The Authors analysed the critical defect size location and found that all defects were within the V_{90}, regardless of the material and defect type. Fig. 1a shows, for each failure, the distance from the specimen centre of the critical defect with respect to the applied stress amplitude in [29] and all the failures were found to be within the V_{90}. In [30], size-effect is investigated by testing hourglass specimens ($V_{90} = 194\ mm^3$) and Gaussian specimens ($V_{90} = 2300\ mm^3$) made of two H13 steels (unrefined H13 steel, H13 in the following, and refined H13 steel, H13-ESR in the following). Failure data have been analysed by considering the local stress ratio associate to each failure, i.e., the ratio between the local stress and the maximum applied stress. In Fig. 1b, the local stress ratio associated to each failure is plotted for each tested steel type. According to the Fig. 1b, all failures apart from one are within the V_{90}.

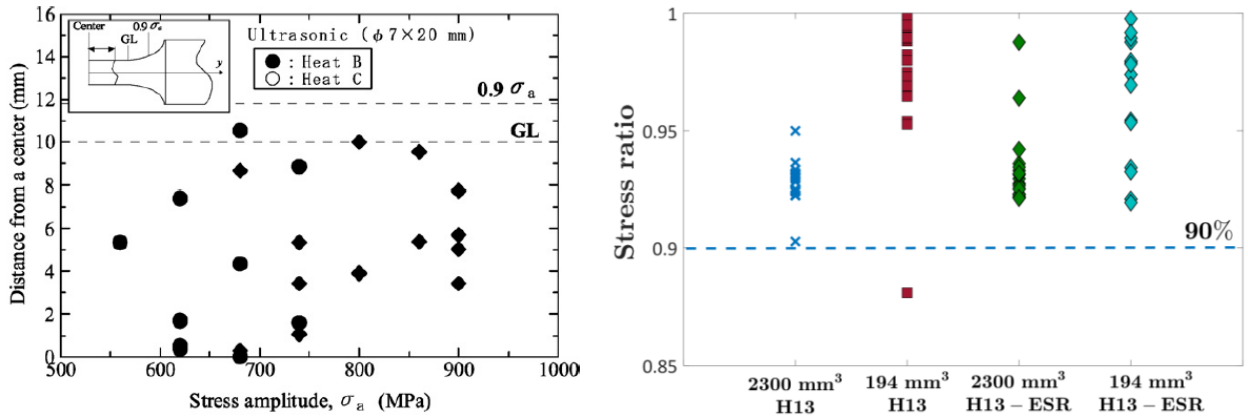

(a) (b)

Figure 1: Defect location in [29] and [30]: a) distance from the specimen center of the critical defect with respect to the applied stress amplitude [25]; b) local stress ratio associated to each critical defect in [30].

The experimental results obtained in [29] and [30] confirmed the effectiveness of employing the V_{90} for the analysis of the experimental data, even in case of ultrasonic fatigue tests. On the other hand, in [31], the Authors showed that the use of the V_{90} as the volume at risk could not be conservative in the VHCF regime. Experimental tests were carried out on hourglass and Gaussian specimens made of a H13-ESR steel with $V_{90} = 55\ mm^3$ and $V_{90} = 5000\ mm^3$, respectively. The experimental results obtained by testing hourglass specimens are used for predicting the VHCF response of the Gaussian specimens with $V_{90} = 5000\ mm^3$. The predicted S-N curve was found to be non-conservatively above the experimental curve. The Authors ascribed this difference to a non-appropriate choice of the volume at risk. Indeed, a specific threshold stress ratio, as the 90% of the maximum applied stress, does not account the influence of the stress distribution and of the stress gradient within the nominal loaded volume. The influence of the stress gradient within the V_{90} can be more significant in ultrasonic VHCF tests than in HCF tests since, in ultrasonic VHCF tests, specimens have non-standard geometries and are characterized by different stress distributions. In addition, the Authors pointed out that defects subjected to a stress amplitude below the 90% of the maximum stress are not critical in HCF tests if the SIF associated to these defects is smaller than threshold for crack propagation. On the other hand, the same defects could become critical in the VHCF region, with the crack nucleation assisted by the well-known mechanisms that induce the formation of the Optically Dark Area (hydrogen) or the Fine Granular Area (FGA). For these reasons, the Authors suggested that the risk-volume should be defined by taking into account also the stress gradient.

In [32-34], a different approach, that does not require an a priori choice of the volume at risk, has been used for modelling volume at risk.

In [32] a probabilistic model for the VHCF fatigue life of spheroidal graphite cast iron is proposed. In particular, a weakest-link based model for the fatigue failures from internal defects is defined: even if VHCF

tests were not carried out, the Authors pointed out that the fatigue response in the VHCF region can be safely extrapolated. The Authors focused on the concept of "effective volume" V_{eff}^{*}, which corresponds to the volume in which the VHCF failure can occur. It is defined as:

$$V_{eff}^{*} = H_{\beta+1}^{*} \cdot V, \tag{5}$$

where V is the component volume and $H_{\beta+1}^{*}$ the so called "*stress heterogeneity factor*", which is dependent on the load type, on the load level, on the defect size, and on the threshold stress for crack propagation. Indeed, the V_{eff}^{*} is equal to 0 when the applied stress is smaller than the threshold stress obtained from the SIF threshold, whereas it is equal to V when the component is subjected to a uniaxial stress distribution. According to the Authors, $H_{\beta+1}^{*}$ "*characterizes the effect of loading patterns on the failure probability*". Indeed, the more uniform is the stress field, the higher is the probability of finding a critical defect, following the definition of volume at risk. In the paper, the effective volume associated to each element with volume V_0 is computed, in order to map the probability of failure associated to each element.

In [33], the experimental data are analysed by considering the "*real volume*", V_{real}, associated to each defect originating the fatigue failure. V_{real} is defined as the "*volume of material subjected to a stress amplitude larger than the stress amplitude evaluated at the inclusion location*". This definition ensures that the inclusion originating failure is the most critical defect within the real volume and permits avoiding an arbitrary choice of the risk-volume or of the stress ratio threshold. This approach enables to properly assess the critical inclusion: indeed, even if larger inclusions are present outside the V_{real}, they are not critical for the VHCF response.

In [34], the Author pointed out that the threshold stress ratio for identifying the risk-volume could be not uniquely defined and depends on different factors, such as the stress gradient and the material. Moreover, depending on the selected specific stress ratio threshold (e.g., the 80% in place of the 90%), the LEVD parameters change. However, this is not physically admissible, since the parameters for the LEVD must be a material constant. For these reasons, an approach based on the stress ratio threshold may lead to an inaccurate assessment of size-effect in VHCF, with possible implications on the design of components against VHCF failures. Therefore, in the paper, size-effect is accounted with no need of defining a risk-volume and by applying the weakest-link principle. Moreover, with the proposed statistical approach, the stress gradient within the highly stressed volume and the interaction between the defect size and the local applied stress (i.e., large defects in a lightly stressed region may be less critical than small defects in a highly stressed region) are accounted. More details about this model and its statistical formulation will be provided in Section 2.4.

According to the above analyses, a unique definition for the risk-volume is not available in the literature. The stress ratio threshold approach has proved to work for many experimental datasets and can be easily applied. However, this approach fails to model the interactions between the defect size, the local stress and the stress

gradient within the volume and the choice of the specific threshold stress ratio to be considered depends on the material and on the manufacturing processes. Moreover, depending on the considered stress ratio, the parameters of the LEVD may vary, even if this is not physical. Therefore, approaches that do not involve an a priori choice of the volume at risk would be more effective and can better assess the probability of failure associated to a component. However, these methodologies can be more difficult to implement, since they are based on statistical models that can be quite complex and would require Finite Element Analyses.

2.3 Size effect in VHCF: fatigue limit

In this Section, the models developed and experimentally validated for the assessment of the fatigue limit in VHCF are analyzed. In particular, the papers that provide a model for the fatigue limit are revised: for the analysis of the finite fatigue life (and of the fatigue limit as an asymptote at the end of the P-S-N curve) the reader could refer to Section 2.4.

In the HCF life range, the dependency between the fatigue limit and the risk-volume can be assessed through the LEVD [8]. In the VHCF region, on the other hand, the estimation of the defect size distribution cannot be sufficient. For example, if the Murakami formulation is considered for the estimation of the fatigue limit in VHCF and the fatigue failures originate with ODA formation, the ODA size must be considered in place of the defect size [8, 22]. Therefore, the dependency between the defect size and the ODA size should also be considered when dealing with size effect in VHCF.

In [22] size-effect is modeled with the so-called “Master curve of ODA”. A procedure for the design against VHCF failure and capable to take into account size-effect is proposed. This procedure will be analyzed in Section 3.1, dedicated to design methodologies against VHCF failures.

In [29] size-effect in VHCF is experimentally verified by testing hourglass specimens (gage diameter 3 mm, $V_{90} = 33\ mm^3$) and dog bone specimens (gage diameter 7 mm and length of the straight section 20 mm, $V_{90} = 912\ mm^3$), made of a JIS-SUP7 spring steel. The geometries of specimens are shown in Fig. 2a. The specimens were subjected to two heat treatments, Heat B and Heat C, employed by the Authors in previous works [35]. The microstructure of the specimens after the two heat treatments was the same, but the defects at the origin of fatigue failures were found to be different in previous works (i.e., oxide-type inclusions for Heat B and TiN, matrix defect and oxide-type inclusions for Heat C). Ultrasonic fatigue tests up to $5 \cdot 10^9$ cycles were carried out by the Authors. The S-N plots of the experimental data are shown in Fig. 2b and 2c for Heat B and Heat C, respectively. Regardless of the heat treatment, failures curves for dog bone specimens were below failures curves for the hourglass specimens. The VHCF strength decrement was due to the increment of defect size with the risk-volume according to the Gumbel plot of the critical defects shown in Figure 2d. The specimens subjected to Heat B failed with cracks initiating from oxide type inclusions, whereas the cracks in specimens subjected to Heat C initiated from TiN, matrix defects and oxide type inclusions. In particular, TiN or matrix inclusions were at the origin of the fatigue failures only in small hourglass specimens

and showed a smaller size. The average oxide-type inclusion sizes in the dog-bone and in the hourglass specimens were $50\ \mu m$ and $29\ \mu m$ for Heat B, and $29\ \mu m$ and $14\ \mu m$ for Heat C, respectively. The largest TiN inclusion or matrix defect in Heat C hourglass specimens was $10\ \mu m$, showing for Heat C also a size-effect related to the defect type. Indeed, large oxide type inclusions were rare and were more likely to be found in large risk-volumes. This result confirms that experimental tests on small specimens would fail to properly assess the defect population, if multiple types of defects are at the origin of the fatigue failures. [8]. The dependency between the fatigue limit and the V_{90} for Heat B was modeled according to the fatigue limit formulation in [8] (Eq. 6) and by considering the defect size computed with the LEVD in Eq. 3:

$$s_l = \frac{1.56\cdot(HV+120)}{(\sqrt{a_{d,0}})^{\frac{1}{6}}}, \tag{6}$$

Figure 2e shows the relation between the fatigue limit and the V_{90} for the Heat B specimens: the estimated model and the experimental VHCF strength at 10^{10} cycles are plotted. The curve is not conservative for the hourglass specimens, whereas it is conservative for the dog bone specimen. The Authors concluded that the model is in agreement with the experimental data. The Authors did not provide details if an ODA was found around the initial defect and considered the initial defect size in Eq. 6 for the computation of the fatigue limit. However, the majority of failures in VHCF shows an ODA around the initial defect: in this case, the Murakami formulation can be applied only by replacing the defect size with the ODA size. Therefore, the results obtained in [29] are valid only for specimens failing from defects without ODA formation.

The decrement of the fatigue limit computed by considering the experimental data for Heat B in Figure 2e was found to be 22%. A similar decrement, about 20%, was found for Heat C by considering the smallest runout stress amplitude for each heat treatment. These experimental results show a significant dependency between the fatigue limit and the VHCF strength.

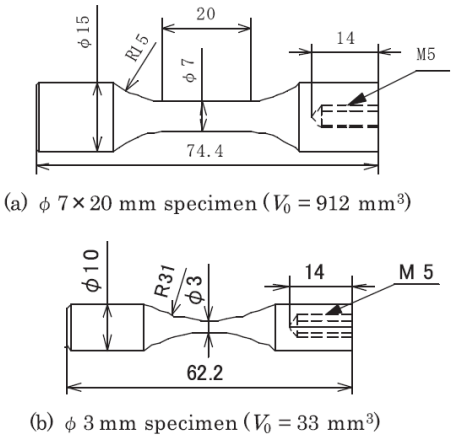

(a) ϕ 7×20 mm specimen (V_0 = 912 mm^3)

(b) ϕ 3 mm specimen (V_0 = 33 mm^3)

(a)

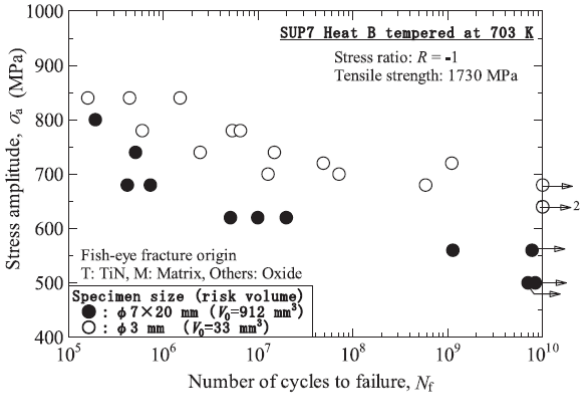

(a) Heat B

(b)

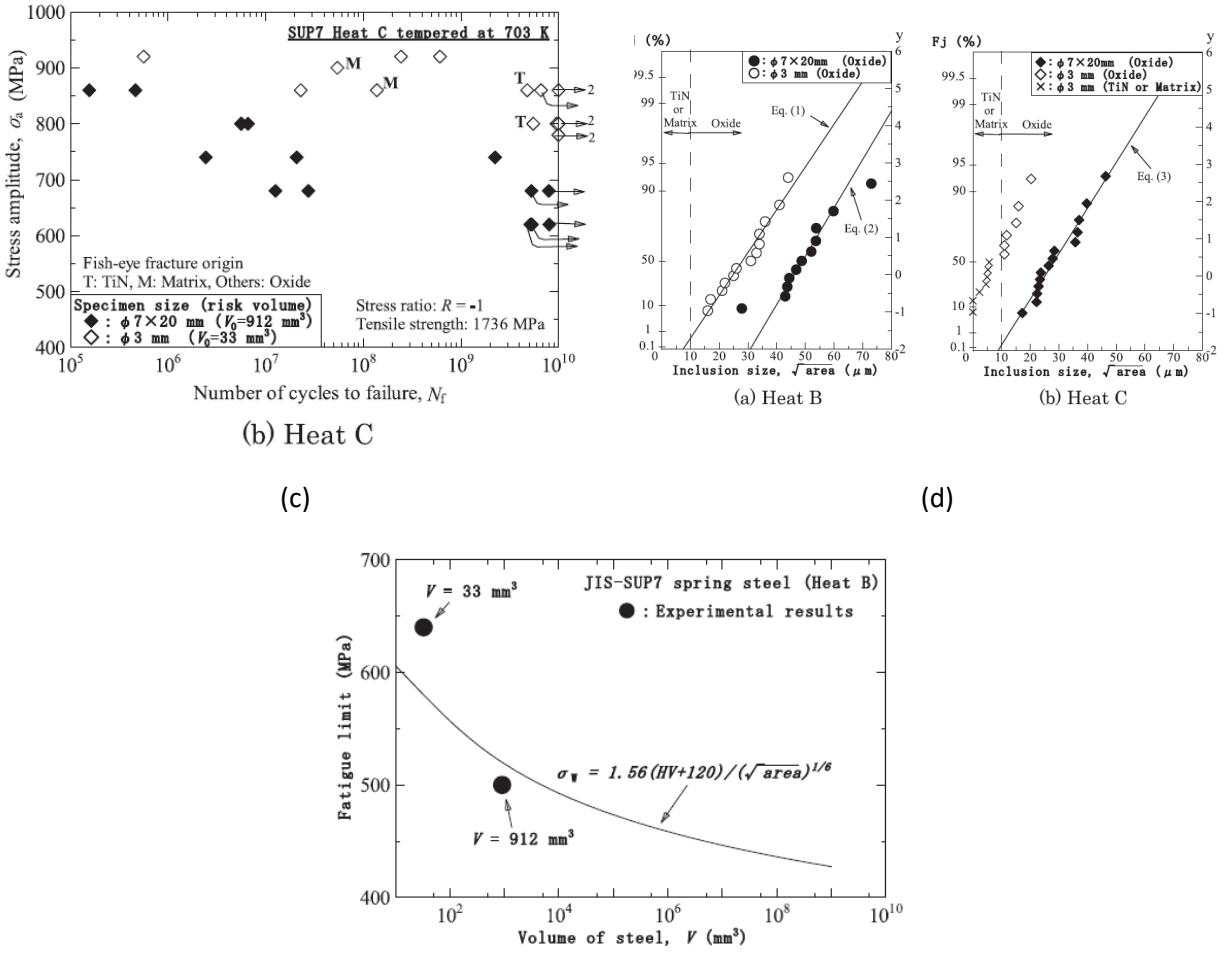

Figure 2: Experimental results in [29]; a) specimen geometry; b) S-N plot of the experimental data for Heat B; c) S-N plot of the experimental data for Heat C; d) Gumbel plot of the critical defect sizes; e) fatigue limit with respect to V_{90}.

In [36], the dependency between the fatigue limit and the inclusion size is assessed, focusing on the influence of the V_{90} for the prediction of the largest inclusion in components. Ultrasonic fatigue tests were carried out up to failure or to 10^9 cycles on dog-bone specimens with $6\,mm$ gage diameter and $16\,mm$ gage length ($V_{90} = 486\,mm^3$) made of 35CrMo steel subjected to quenching and tempering. A group of specimens was nitrocarburized (*treated specimens* in the following), whereas another group of specimens was only mechanically polished (*untreated specimens* in the following). All the fatigue failures in the VHCF region originated from internal defects, mainly oxide type inclusions, with a fish-eye fracture morphology. The Authors did not specify if an ODA was found close to the initial defect. The largest defect was equal to $50\,\mu m$ and the $\sqrt{a_{d,0}}$ for each internal failure was measured and assumed to follow a LEVD. The parameter estimation for the LEVD was computed by applying the Maximum Likelihood Principle and by considering the critical defects. According to Eq. 3, the expected defect in a $V_{90} = 108839\,mm^3$, corresponding to the risk-

volume of axles of the high-speed train "China Star", was found to be equal to $111\ \mu m$. Given the dependency between the inclusion size and the V_{90}, the fatigue limit was predicted according to the formulation:

$$s_l = \frac{\Delta K_{th,I}}{0.5\sqrt{\pi \cdot \sqrt{a_{d,0}}}}, \tag{7}$$

where $\Delta K_{th,I}$ is the Stress Intensity Factor (SIF) threshold for an internal failure. The fatigue limit for a surface inclusion was also estimated by replacing $\Delta K_{th,I}$ with $\Delta K_{th,S}$ and coefficient 0.5 with 0.65. $\Delta K_{th,I}$, estimated by the Authors in previous works, was equal to $3.1\ MPa \cdot \sqrt{m}$. Figure 3 plots the fatigue limit (for surface and internal defects) with respect to the inclusion size. It is worth noting that by replacing Eq. 3 in Eq. 7 the dependency between the fatigue limit and the defect size can be easily obtained.

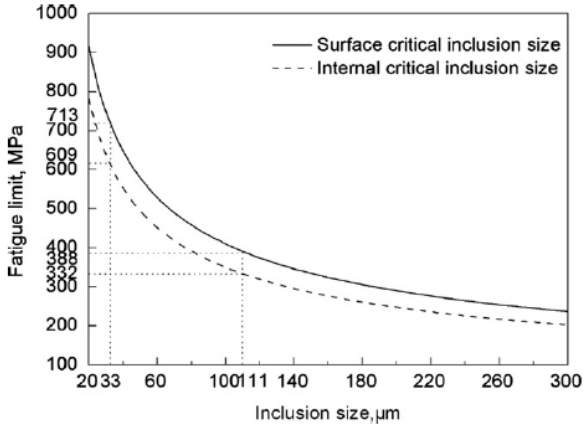

Figure 3: Dependency between the fatigue and the defect size (implicit dependency between the fatigue limit and the V_{90}) in [36].

According to Fig. 3, the decrement for the fatigue limit with respect to the inclusion size (and, accordingly, with the V_{90}) is rapid for defects smaller than $60\ \mu m$ ($V_{90} = 486\ mm^3$), whereas above $60\ \mu m$ the slope of the curve tends to decrease. According to the Authors, the fatigue strength for an internal defect reduces from $495\ MPa$ for $V_{90} = 486\ mm^3$ to $332\ MPa$ for $V_{90} = 108839\ mm^3$, with a 32% decrement. The Authors confirmed that the predicted fatigue strength is close to that estimated in the literature by testing a full-scale component made of 30NiCrMoV12 steel with similar mechanical properties.

As for the results in [29], these considerations are limited to cracks which originate from a defect without ODA formation.

According to [29] and [36], the experimental tests should be carried out on specimens with the largest possible V_{90}. However, a significant increment of the V_{90} in ultrasonic fatigue tests is limited, even in dog-bone specimens, due to the non-uniform stress distribution in the gage length with constant cross-section (i.e., the specimens work in resonance conditions and the applied stress depends on the longitudinal stress wave propagation through the material). In order to increase the V_{90} that can be tested through the ultrasonic fatigue tests, the research group [19, 23] of Politecnico di Torino proposed a new type of specimen,

called "*Gaussian specimen*". The specimen geometry is similar to that of traditional dog-bone specimens, but the gage length has a profile described by a Gaussian function, obtained by solving the equation for longitudinal wave propagation and imposing a constant stress amplitude [19]. The stress amplitude within the specimen risk-volume has been validated with strain gages and through Finite Element Analyses (FEAs). The effectiveness of the proposed specimen shape was verified in [23], showing that the Gaussian specimen permits not only to increase the risk-volume, but also to obtain a constant stress amplitude close to the maximum applied stress. The Gaussian specimens have been used by the research group of Politecnico di Torino to assess size-effect on VHCF.

In [33], size-effect on the VHCF response of an H13-ESR tool steel has been experimentally assessed. Ultrasonic fully-reversed tension-compression tests were carried out with two ultrasonic fatigue testing machines. Hourglass specimens (gage diameter 6 mm and $V_{90} = 194\ mm^3$) and Gaussian specimens (gage diameter $11\ mm$ and $V_{90} = 2300\ mm^3$) were tested. The specimen geometry is shown in Figure 4a. In the paper, the influence of size-effect on the VHCF response is assessed by considering the real volume, V_{real} (Section 2.2, defined as the "*volume of material subjected to a stress amplitude larger than the stress amplitude evaluated at the inclusion location"*). The dependency between the fatigue limit and V_{real} is assessed by exploiting the statistical distribution of the marginal fatigue limit $F_{X_l}(x_l)$, i.e., the fatigue limit not conditioned to the defect size, defined in [33] as:

$$F_{X_l}(x_l) = \int_0^\infty F_{X_l|\sqrt{a_{d,0}}}\left(x_l; \sqrt{a_{d,0}}\right) \cdot f_{\sqrt{A_{d,0}}}\left(\sqrt{a_{d,0}}\right) d\sqrt{a_{d,0}} \tag{8}$$

where $F_{X_l|\sqrt{a_{d,0}}}\left(x_l; \sqrt{a_{d,0}}\right)$ is the cumulative distribution function (cdf) of the conditional fatigue limit, assumed to be normally distributed with mean dependent on the defect size ($\mu_{X_l}\left(\sqrt{a_{d,0}}\right) = \frac{c_{sl} \cdot c_{th} \cdot (HV+120)}{\left(\sqrt{a_{d,0}}\right)^{0.5-\alpha_{th}}}$, where c_{sl}, c_{th} and α_{th} are constant coefficients to be estimated from the experimental data) and constant standard deviation, and $f_{\sqrt{A_{d,0}}}\left(\sqrt{a_{d,0}}\right)$ is the probability density function (pdf) of the LEVD. By expressing the LEVD as a function of the V_{real}, the dependency between the fatigue limit and V_{real} can be assessed. Moreover, differently from the analyses in [29, 36], the parameter estimation was carried out by considering the FGA size measured on the fracture surfaces. Indeed, the c_{sl} coefficient was estimated by maximizing the likelihood function expressing the probability of having a failure or a runout for the experimental dataset, whereas the c_{th} and α_{th} are estimated through a linear regression between the SIF threshold and the FGA size. Therefore, with the proposed method, the FGA size is taken into account. In Fig. 4b, the fatigue limit with respect to the real volume is plotted.

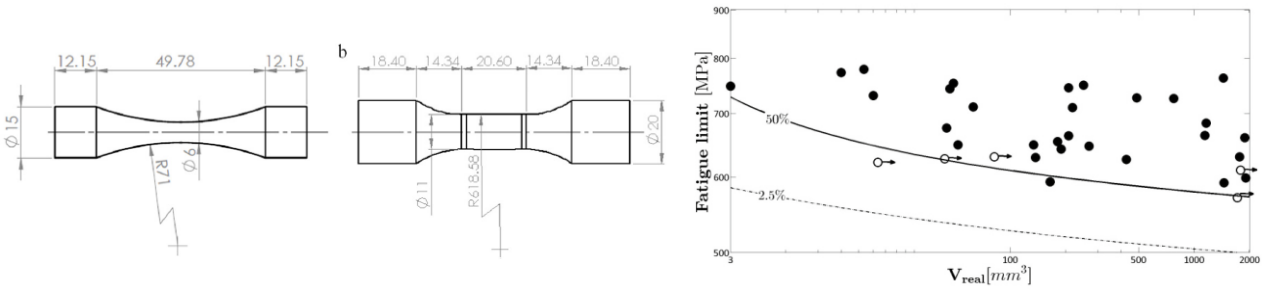

(a) (b)

Figure 4: Experimental results in [33]; a) specimen geometry; b) fatigue limit with respect to the real volume.

According to Fig. 4b, the proposed model is in agreement with the experimental data, with all the fatigue failures except one above the median curve and no failures below the 0.025-th quantile curves. The fatigue limit decreases with V_{real}, with a 21% decrement from the smallest V_{real} ($3\ mm^3$) to the largest V_{real} ($1914\ mm^3$). The model in [33] enables to properly assess the dependency between V_{real} and the fatigue limit and the use of the V_{real} in place of the V_{90} enables to accurately assess the actual volume involved in the crack nucleation process, since the estimated model is in agreement with both the experimental results obtained by testing hourglass and Gaussian specimens.

In [38], the model defined in Eq. 8 has been exploited to assess the dependency between the fatigue limit and the V_{90}. Experimental tests have been carried out on Gaussian specimens with the geometry shown in Fig. 4a made of an H13 steel. The constant coefficients have been estimated by considering the SIF threshold trend with respect to the FGA size and by minimizing the difference between the experimental and the analytical number of cycles consumed within the FGA. The estimated fatigue limit variation with respect to the V_{90} is shown in Fig. 5. The model is agreement with the experimental data, with all the failures conservatively above the median curve.

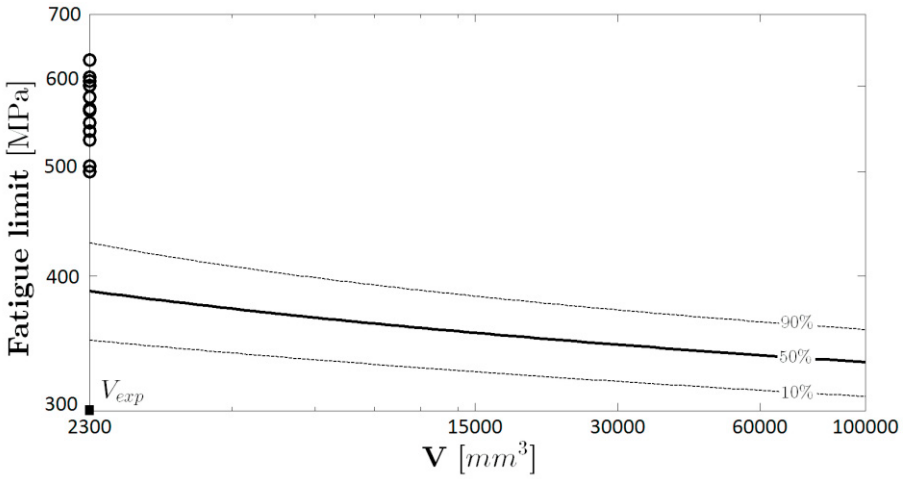

Figure 5: fatigue limit with respect to the V_{90} in [38].

In [39], experimental tests have been carried out on hourglass specimens with the geometry reported in Fig. 4a made of H13 and H13-ESR steels. The dependency between the fatigue limit with respect to the V_{90} is obtaind according to the model in Eq. 8 and the parameter estimation has been carried out by applying the Maximum Likelihood Principle, according to [40]. The objective of the paper was to verify if the fatigue limit trend with respect to the V_{90} can be properly estimated through tests on small specimens, like the tested hourglass specimens. The fatigue limit variation with respect to the V_{90} for the H13 and the H13-ESR steels is shown in Fig. 6, together with the experimental fatigue limit for the Gaussian specimens.

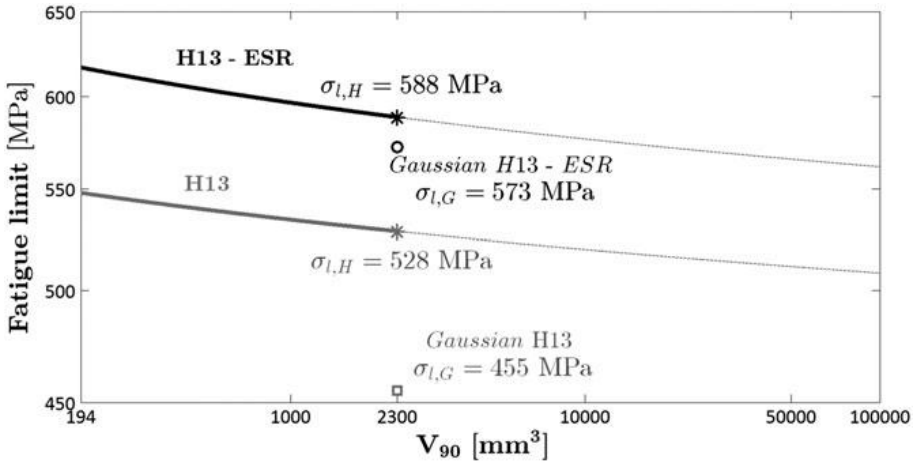

Figure 6: Fatigue limit with respect to the V_{90} in [39] estimated with the experimental results of tests on hourglass specimens.

According to Fig. 6, the predicted VHCF limits are unsafely above the experimental values for both the H13 and the H13-ESR steels. The difference is larger than 16% ($73\ MPa$) for H13 steel, whereas it reduces to 2.6% for H13-ESR ($15\ MPa$). These results suggest that the prediction of the fatigue limit through tests on small specimens may not be conservative. However, for the H13-ESR the difference is limited and by considering a quantile with high reliability, a safe prediction can be obtained. On the other hand, for the not refined H13 steel, the difference is significant, suggesting that the steel cleanliness plays an important role in size effect.

2.4 Size effect in VHCF: finite fatigue life

In this Section the influence of size-effect on the finite fatigue life is investigated. In [25, 41], tests are carried out on two types of hourglass specimens, with $3\ mm$ gage diameter ($V_{90} = 33\ mm^3$) and $7\ mm$ gage diameter ($V_{90} = 254\ mm^3$) and on dog-bone specimens with $8\ mm$ diameter and gage length of $10\ mm$ ($V_{90} = 781\ mm^3$). The specimens were made of an IS-SCM440 (AISI-4140) low alloy steel, with the geometry shown in Fig. 7a and Fig. 7b. Ultrasonic fully reversed tests were carried out: the validity of the ultrasonic fatigue tests was also verified. The experimental results are reported in an S-N plot (Fig. 7c), that shows that the VHCF strength decreases with the risk-volume. By comparing the VHCF strengths at $5 \cdot 10^9$ cycles for the

3 mm hourglass specimens and for the dog-bone specimens, the decrement was about 25%. The Authors do not provide details about the calculation of the VHCF strength at $5 \cdot 10^9$ cycles.

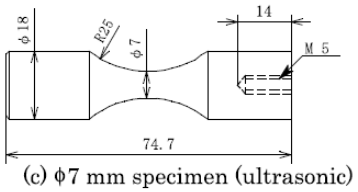

(c) ϕ7 mm specimen (ultrasonic)

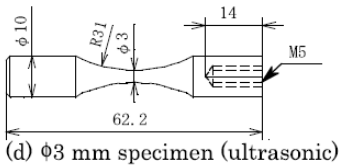

(d) ϕ3 mm specimen (ultrasonic)

(a)

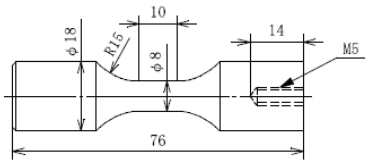

(a) ϕ8×10 mm specimen (ultrasonic)

(b)

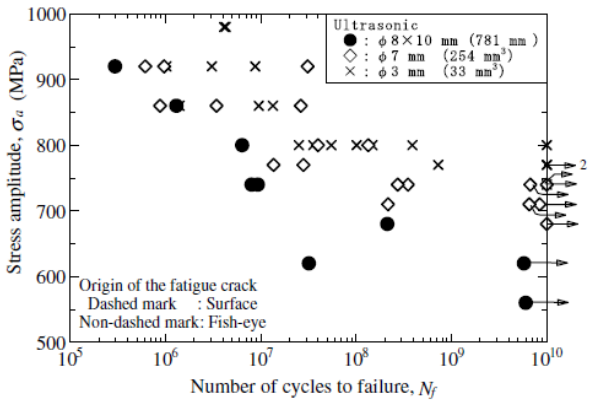

(c)

Figure 7: Experimental results in [25]; a) hourglass specimen geometries; b) dog-bone specimen geometry; c) S-N plot of the experimental data.

In [40], the marginal P-S-N curves were considered for the assessment of size effect on the VHCF life. As for the fatigue limit, they are called marginal since they are estimated by considering the LEVD, with constant coefficients estimated by considering the critical defect sizes:

$$F_{Y|int}(y;x) = \int_0^{\infty} F_{Y|\sqrt{a_{d,0}}}(y;x,\sqrt{a_{d,0}}) f_{\sqrt{A_{d,0}}}(\sqrt{a_{d,0}}) d\sqrt{a_{d,0}}, \quad (9)$$

where $F_{Y|int}(y;x)$ is the marginal distribution of the fatigue life (y and x are the logarithm of N_f and of the s_a, respectively), $F_{Y|\sqrt{a_{d,0}}}(y;x,\sqrt{a_{d,0}})$ the conditional fatigue life (i.e., the fatigue life for a specific defect size), modelling a linear decreasing trend ending with an asymptote. By expressing the dependency between the LEVD and the risk-volume (Eq. 3), Eq. 9 enables to estimate the P-S-N curves as a function of the risk-volume.

In [30], all the experimental results on the H13 and H13-ESR steels, hourglass and Gaussian specimens ($V_{90} = 194\ mm^3$ and $V_{90} = 2300\ mm^3$, respectively) were analyzed to assess the influence of size-effect on the P-S-N curves. The estimated marginal 0.01-th quantile P-S-N curves are shown in Fig. 8. In the Figure, the letter "h" refers to the hourglass specimens, whereas "G" refers to "Gaussian specimens": for example, H13-ESR G refers to the Gaussian specimens made of H13-ESR steel.

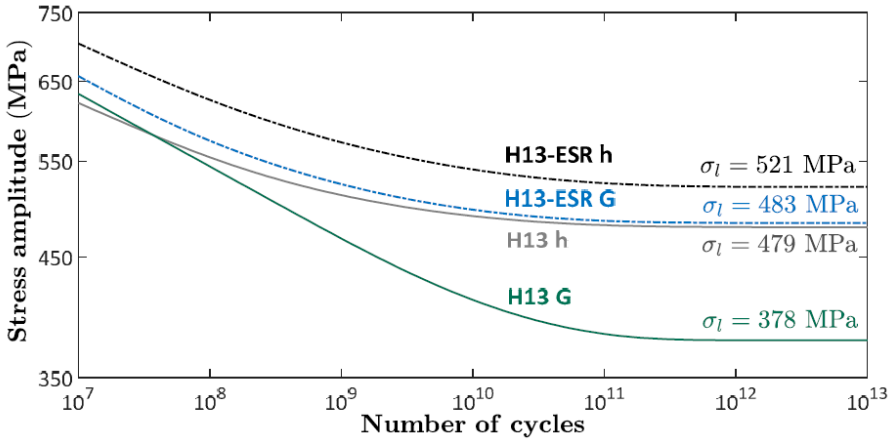

Figure 8: Marginal P-S-N curves estimated in [30]: effect of the specimen volume and of the steel cleanliness.

According to Fig. 8, two behaviors are found, depending on the steel cleanliness. For the H13-ESR, the difference between the P-S-N curve estimated by testing the hourglass specimens and the Gaussian specimen is constant throughout the VHCF life, about $40\ MPa$. On the contrary, it increases with the number of cycles for H13 steel, reaching a maximum difference of $105\ MPa$ above 10^{11} cycles, where the curves show an asymptotic trend. According to these results, for materials with high sensitivity to defect size with the risk-volume, size-effect could vary depending on the number of cycles to failure. Indeed, for the H13 steel, size-effect has a larger influence at very high number of cycles, where the influence of defects on the VHCF response is prevalent. Therefore, these results confirm that the enhancement of the steel cleanliness can be an appropriate strategy to limit size-effect.

In [31], size-effect was further analyzed by testing hourglass and Gaussian specimens characterized by a $V_{90} = 33\ mm^3$ and a $V_{90} = 5000\ mm^3$. The specimens were made of H13-ESR steel, but machined from a base material with mechanical properties and microstructure different from that tested in [30]. The Authors experimentally verified the capability of predicting the VHCF response of parts with large V_{90} by considering the experimental results obtained through tests on small specimens. Figure 9 shows the experimental and the predicted median P-S-N curves: the $V_{exp} = 33\ mm^3$ and the $V_{exp} = 5000\ mm^3$ P-S-N curves were estimated from the experimental data, whereas the $V_{pred} = 5000\ mm^3$ P-S-N curve is the one predicted by considering the test results on hourglass specimens and by applying Eq. 9 (i.e., the constant parameters in the model have been estimated from the test results on hourglass specimens).

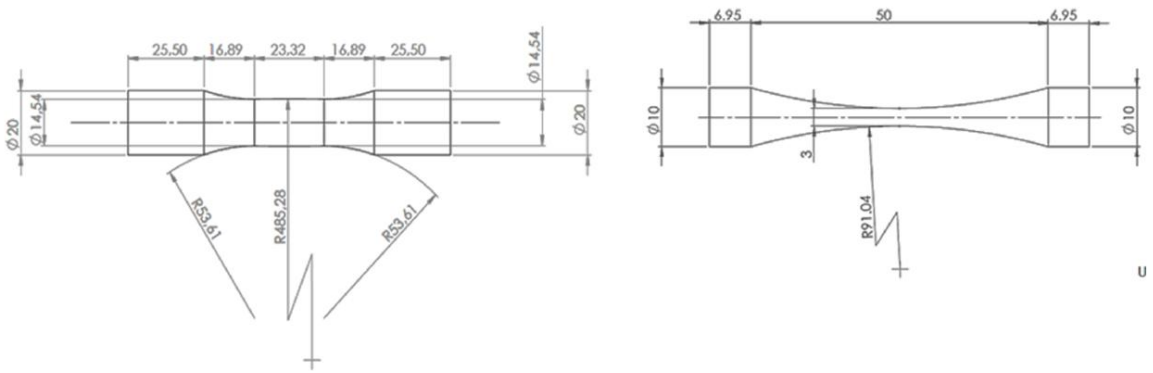

(a)

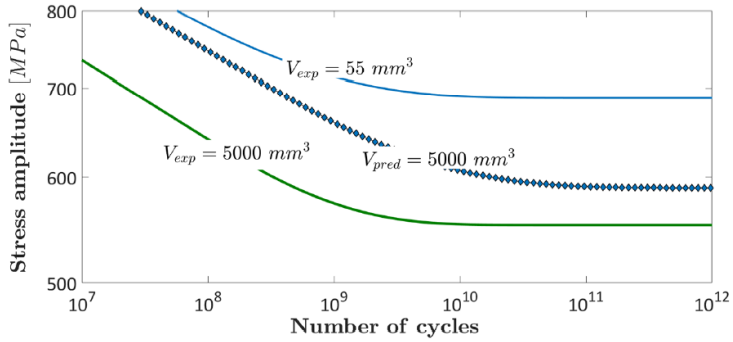

(b)

Figure 9: Experimental results in [31]: a) specimen geometries; b) experimental and predicted P-S-N curves.

As shown in Fig. 9, size-effect induces a significant decrement of the VHCF response: the experimental curve for the hourglass specimens was above the experimental curve for the Gaussian specimens, with an almost constant difference of $140\,MPa$ (about 20% reduction at 10^{11} cycles). The predicted curve is non-conservatively above the experimental curve for the Gaussian specimens. The Authors pointed out that the main reason for this difference is that the LEVD cannot properly predict the largest defect and that a risk-volume defined by considering a stress threshold ratio fails to account the real volume involved in the crack nucleation process and the influence of the stress gradient in the volume, as discussed in Section 2.2.

In [42], a weakest-link approach is employed for modelling the influence of size-effect on the VHCF life. According to the Authors, the monotonic decreasing trend observed in the LCF-HCF region continues in the VHCF region, with no transition stress and change in the curve slope. Basquin's model has been employed to model the stress-life relation, with the fatigue life, $log_{10}(N_f)$, assumed to follow a Weibull distribution. The dependency between the specimen volume, V_{90}, and the fatigue life is modelled with a weakest-link approach. Indeed, the Authors assumed that large specimens (or large components) can be considered as composed by n small specimens that are generally tested in the lab. According to the weakest-link principle, the fatigue life distribution for a large specimen, $F_{N^L}(x)$, composed by n small specimens, is the minimum among the fatigue life of n small specimens:

$$F_{N^L}(x) = 1 - [1 - F(x)]^n \text{ with } F(x) \begin{cases} 1 - e^{-(x/\lambda)^k} & x \geq 0 \\ 0 & x \geq 0 \end{cases} \quad (10)$$

where $F(x)$ is the cdf of the fatigue life of small specimens, λ and k constant parameters to be estimated from the experimental data. According to the Authors, the distribution of the fatigue life does not depend on the specimen size. Differently from the other methods analyzed above, size-effect is modelled without taking into account the defect size or the defect size distribution, but through a statistical approach based on the assumption of the statistical distribution of the fatigue life and on a weakest-link approach. The model has been validated with literature datasets [25, 29]. Figures 10a and 10b show the P-S-N curves for the dog-bone specimens ($V_{90} = 912\ mm^3$). Curves are predicted by considering the experimental results of tests on small hourglass specimens ($V_{90} = 33\ mm^3$) for a JIS-SUP7 subjected to the Heat B and Heat C, respectively [29]. Figures 10c and 10d show the experimental results in [25] and the P-S-N curves predicted by considering the experimental results of tests on hourglass specimens ($V_{90} = 33\ mm^3$) made of a JIS-SCM440 steel. In Fig. 10c, the model is validated by considering the experimental results of tests on specimens with $V_{90} = 254\ mm^3$, whereas in Fig. 10d the model is validated by considering the experimental results of tests on specimens with $V_{90} = 781\ mm^3$.

According to the Authors, the predicted curves are in agreement with the experimental results obtained by testing large specimens, with the median curve close to the experimental failures and below data for hourglass specimens and the curves with high reliability (i.e., the 0.001-th quantile) below all the experimental failures.

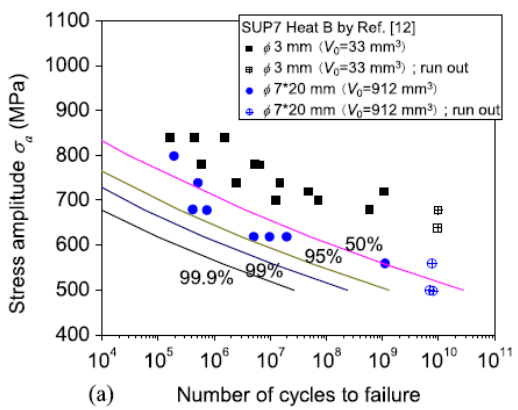

(a)

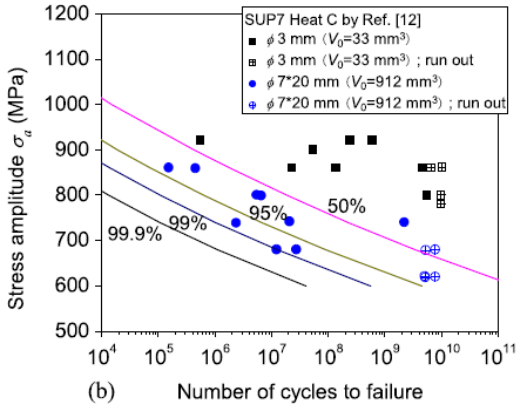

(b)

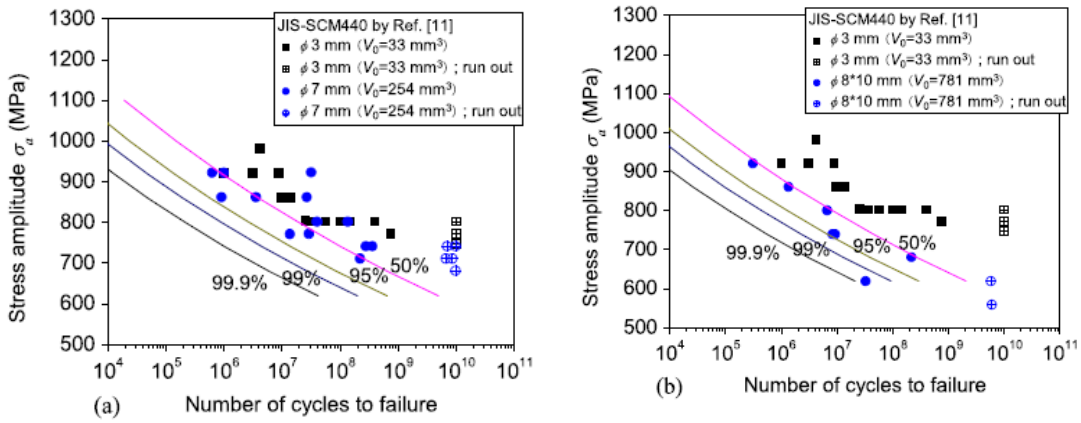

(c) (d)

Figure 10: validation of the model in [42]: a) validation on the literature dataset in [29], Heat B; b) validation on the literature dataset in [29], Heat C; c) validation on the literature dataset in [25], hourglass specimens with $V_{90} = 254\ mm^3$; d) validation on the literature dataset in [25], dog-bone specimens with $V_{90} = 781\ mm^3$.

The P-S-N curves for a full-scale railway axle ($V_L = 35529.5\ mm^3$) have been predicted from the experimental data obtained by testing small specimens ($V_S = 1.260\ mm^3$). The experimental data, together with the P-S-N curves for small specimens and the predicted P-S-N curves (for full-scale railway axle) [42] are shown in Fig. 11. According to the Authors, the decrement is significant, with the fatigue strength of the full-scale railway axles at 10^6 cycles 34% lower (50% reliability) and 33% lower (90% reliability) than that of the small specimens (diameter of $4\ mm$). Moreover, the decrement predicted with the model in [42] was found in agreement with the experimental data on full-scale railway axles [43]. It is worth noting that this validation has been done by considering HCF results. However, since the estimated curves show a monotonic decreasing trend, it can be assumed that this validation is confirmed also in the VHCF life range.

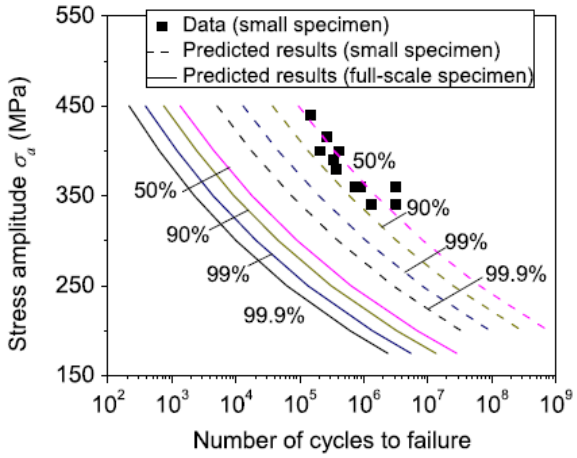

Figure 11: Model in [42] and validation on full-scale railway axles: P-S-N curves predicted for full-scale component ($V_L = 35529.5\ mm^3$) by considering the experimental results obtained by testing specimens with $V_s = 1.260\ mm^3$.

In [44], size-effect on the VHCF response of AlSi10Mg specimens produced through the Selective Laser Melting (SLM) process is investigated. In particular, ultrasonic fully reversed tension-compression tests were carried out on hourglass and Gaussian specimens with V_{90} similar to those tested in [30]. The geometries of hourglass ($V_{90} = 250\ mm^3$ and gage diameter $6\ mm$) and Gaussian specimens ($V_{90} = 2330\ mm^3$ and gage diameter $11\ mm$) are shown in Fig. 12a and 12b, respectively. Experimental tests were carried out on specimens produced in horizontal and vertical direction. All the fatigue failures originated from defects that typically form during the SLM process, like pores, improper layer bonding defect, defect due to incomplete fusion and irregular surface defect. A significant size-effect was found for the defect size for both building orientations: for the horizontal specimens, the largest defect in hourglass specimens was about the 60% of the largest defect in Gaussian specimens; whereas, for vertically built specimens the largest defect in Gaussian specimens was about twice the largest defect in hourglass specimens. The effect of the defect size increment on the VHCF life was investigated: Figure 12c and d show the median and the 0.001-th quantile P-S-N curves, together with the experimental data, for the horizontally built (Fig. 12c) and vertically built (Fig. 12d) specimens. In Fig. 12c and d, the first letter refers to the specimen type ("H" for hourglass and "G" for Gaussian), whereas the second letter refer to the building orientation ("H" for horizontal and "V" for vertical).

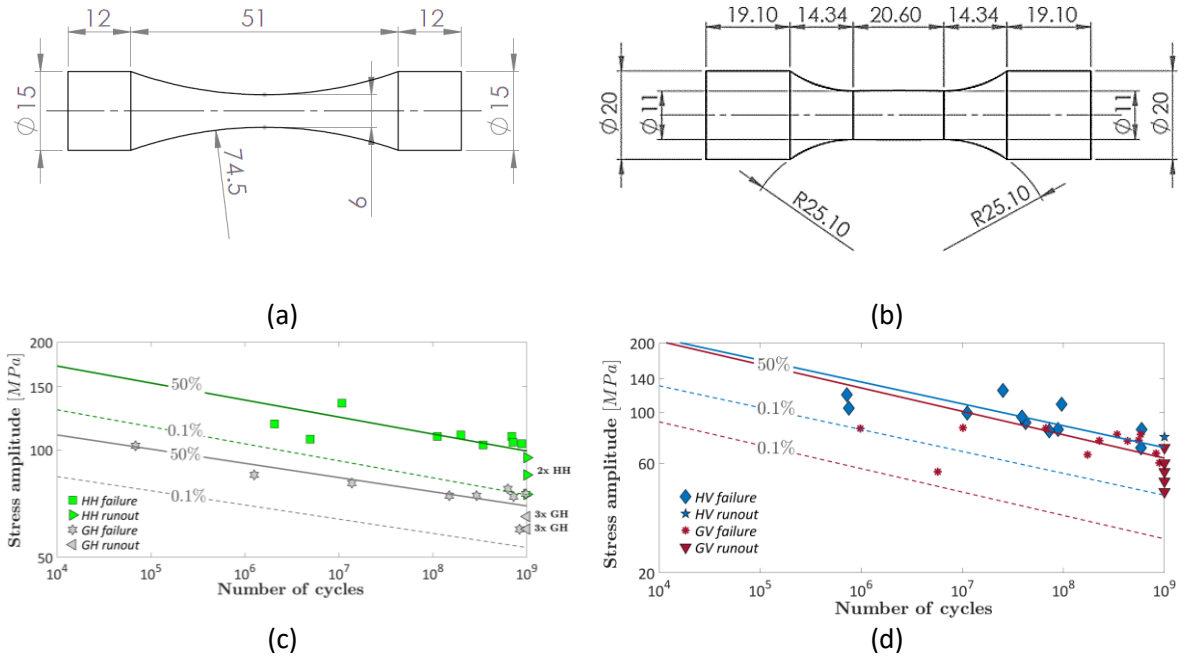

Figure 12: Experimental results in [44]; a) hourglass specimen geometry; b) Gaussian specimen geometry; c) S-N plot of the experimental data and estimated P-S-N curves for the horizontally built specimens; d) S-N plot of the experimental data and estimated P-S-N curves for the vertically built specimens.

According to Figs. 12c and 12d, a significant size effect was also found for the specimens produced with the SLM process. The P-S-N curves for the hourglass specimens are above the curve for the Gaussian specimens, regardless of the building orientation. If the runout N_f is considered, a 30% VHCF strength reduction was found for the horizontal specimens and a 17% VHCF reduction for the vertically built specimens by considering the median P-S-N curve. On the other hand, if the 0.001-quantile curves are considered, a 28% VHCF strength reduction for the horizontal specimens and a large 40% VHCF strength reduction for the vertically built specimens were found. The large reduction for the vertically built specimens and for the 0.001-th quantile is due to the large scatter of the VHCF failures, mainly associated to the large defect increment with the V_{90} for this building orientation. These results confirmed that size-effect is relevant also for AM parts and it can be even larger than that for traditionally built parts, due to the larger defect size range. Furthermore, these results pointed out the importance of taking into account the statistical scatter associated to the VHCF response when dealing with size-effect, especially if components have to be designed.

Finally, in [34], a model for dealing with size-effect without the need of defining a risk-volume is defined. The model has been introduced in Section 2.2: in this Section more details on the statistical methods behind this approach are provided. In particular, the cdf of the fatigue life introduced in Eq. 8 [40] has been rewritten by considering a uniformly stressed volume v_i subjected to a constant stress s_i:

$$F_{Y_i}(y; s_i, v_i) = \int_0^\infty \phi_G\left(\frac{y-\mu_{Y,i}(s_i,\sqrt{a})}{\sigma_Y}\right) f_{\sqrt{A}_i}(\sqrt{a}, v_i) d\sqrt{a}. \quad (11)$$

where $\phi_G\left(\frac{y-\mu_{Y,i}(s_i,\sqrt{a})}{\sigma_Y}\right)$ is the cdf of the conditional fatigue life, assumed to be normally distributed with mean dependent on s_i and on the defect size, $\sqrt{a}$, and constant standard deviation, and $f_{\sqrt{A}_i}(\sqrt{a}, v_i)$ the pdf of the LEVD associated to the volume v_i.

According to the weakest-link principle, the VHCF life of the whole loaded volume is the smallest VHCF life among the VHCF lives related to all the uniformly stressed volumes. The cdf of the smallest VHCF life can be computed from the product of the reliabilities associated to each volume:

$$F_Y\left(y; (s_1, v_1), \dots (s_{n_s}, v_{n_s})\right) = 1 - \prod_{i=1}^{n_s} R_{Y_i}(y; s_i, v_i), \quad (12)$$

where $R_{Y_i}(y; s_i, v_i) = 1 - F_{Y_i}(y; s_i, v_i)$ is the reliability related to the i-th volume v_i. According to Eq. 12, the cdf of the marginal VHCF life for the whole loaded volume depends on all the couples (s_i, v_i), where $i = 1, \dots, n_s$, with n_s the total number of uniformly stressed volumes, that can be computed through a Finite Element Analysis.

The proposed model has been validated on literature datasets and compared with the traditional LEVD approach. In particular, data coming from tests carried out on specimens with different risk-volumes can be plotted together on a Gumbel plot, provided that they are shifted according to Eq. 3 by considering the risk-volume, and are expected to follow a linear trend. The Author validated the model by comparing the coefficient of determination obtained with the model reported in the paper [34] (Eq. 12) and the one obtained by considering all the data together in a Gumbel plot. Figure 13a plots the variation of the coefficients of determination, R_Y^2 and $R_{\sqrt{A_c}}^2$, computed from Quantile-Quantile (Q-Q) plots of the estimated with respect to the experimental values at different stress ratio thresholds (i.e., by considering the volume above a specific stress ratio threshold, s/s_{max}, where s_{max} is the maximum applied stress). In Figure 13a, "Traditional" refers to the traditional approach with the LEVD, whereas "New" refers to the approach proposed by the Author [34]. The superscript Y refers to the estimated VHCF life, whereas the superscript $\sqrt{A_c}$ refers to the defect size. The experimental data considered in this plot have been retrieved from [34]. Fig. 13b shows the Q-Q plot, obtained by considering a stress ratio threshold equal to 70%, of the critical defect size: $\sqrt{A_{c,exp}}$ is the critical defect size found experimentally, whereas $\sqrt{A_{c,est}}$ is the one estimated with the model in [34].

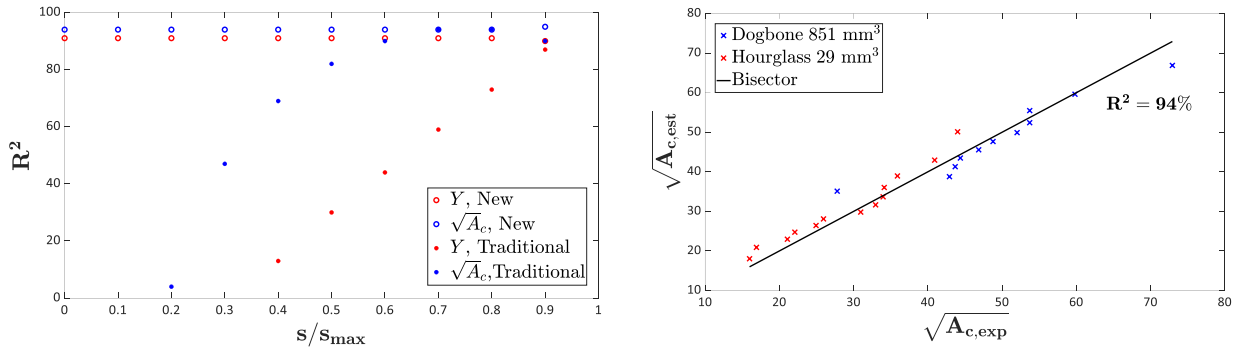

(a) (b)

Figure 13: Model for size-effect in VHCF in [34]; a) coefficient of determination with respect to the threshold stress ratio; b) Q-Q plot of the critical defect size.

According to Fig. 13, the model proposed in [34] enables a proper fitting of the experimental data obtained by testing specimens with different sizes. For all the investigated stress ratio thresholds, the proposed approach is better or equal than the traditional approach. The Q-Q plot in Fig. 13b further confirms the effectiveness of the methdology, with the experimental data close to the bisector.

2.5 Size effect in VHCF: diameter effect

This Section focuses on the investigations of papers that analyse size-effect in VHCF by considering the specimen diameter (or cross-section) as the most influencing parameter, in place of the risk-volume. In [45],

the Authors developed a method for the estimation of the P-S-N curves in the VHCF region based on the analysis of the crack formation and propagation stages from the initial defect. The stress-life relation is obtained by integrating the Paris law from the internal defect to the FGA border and from the FGA border up to the final failure. The coefficients involved in the Paris law are estimated by minimizing the differences between the experimental and the analytical N_f. The Authors validated the model on experimental results obtained by testing bearing steels JIS, SUJ2 and a low-alloy steel, JIS SNCM439. According to the Authors, the model is also capable to assess the dependency between the specimen diameter and the VHCF life. Fig. 14 shows the influence of the specimen diameter on the VHCF life for an inclusion with size equal to $5.6\ \mu m$ and located at $100\ \mu m$ from the surface. However, the Authors do not clarify how the dependency between the diameter and the VHCF strength is modeled, but it is probably accounted by considering the reduction of the stress gradient with the diameter.

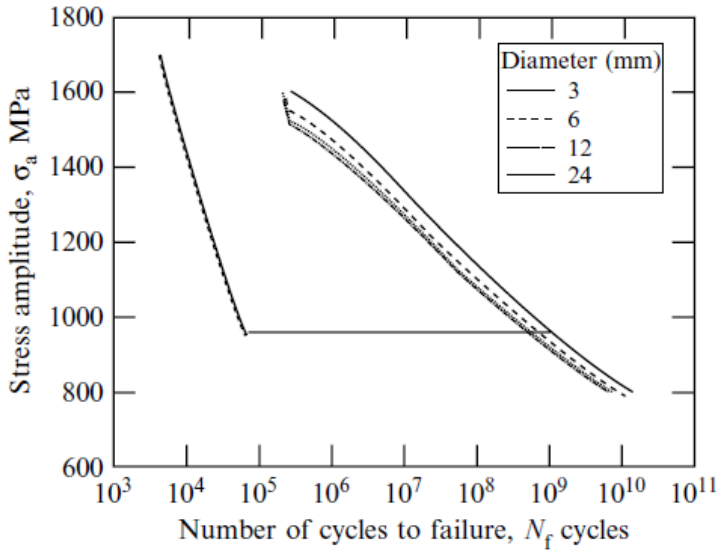

Figure 14: Model for size-effect in VHCF in [45]: P-S-N curve variation with the diameter.

According to Fig. 14, the VHCF strength decreases with the specimen diameter. A larger decrement is observed from $3\ mm$ to $6\ mm$ (from $858\ MPa$ to $832\ MPa$, $26\ MPa$, about 3% at $5 \cdot 10^9$ cycles), whereas it is negligible from the $12\ mm$ to $24\ mm$, with the curves overlapping. This model suggests that size-effect tends to decrease with the diameter. Moreover, the decrement is smaller than that observed for the specimens tested in [29, 30]. However, no validation was carried out to prove the effectiveness of the model. Xue et al. [46] carried out fully reversed ultrasonic fatigue tests on Al-Si-Cu cast alloy hourglass specimens with different gage diameters. In particular, the experimental tests were carried out up to 10^{10} cycles on hourglass specimens with 3 mm and 6 mm gage diameter. The geometry of the tested specimens is shown in Fig. 15a. Conventional fatigue tests were also carried out at a loading frequency of 35 Hz to validate the experimental results obtained with the ultrasonic testing machines. The S-N plot of the experimental dataset

in [46] is shown in Fig. 15b. The experimental data in [46] have been retrieved from the S-N plot by using the software Engauge.

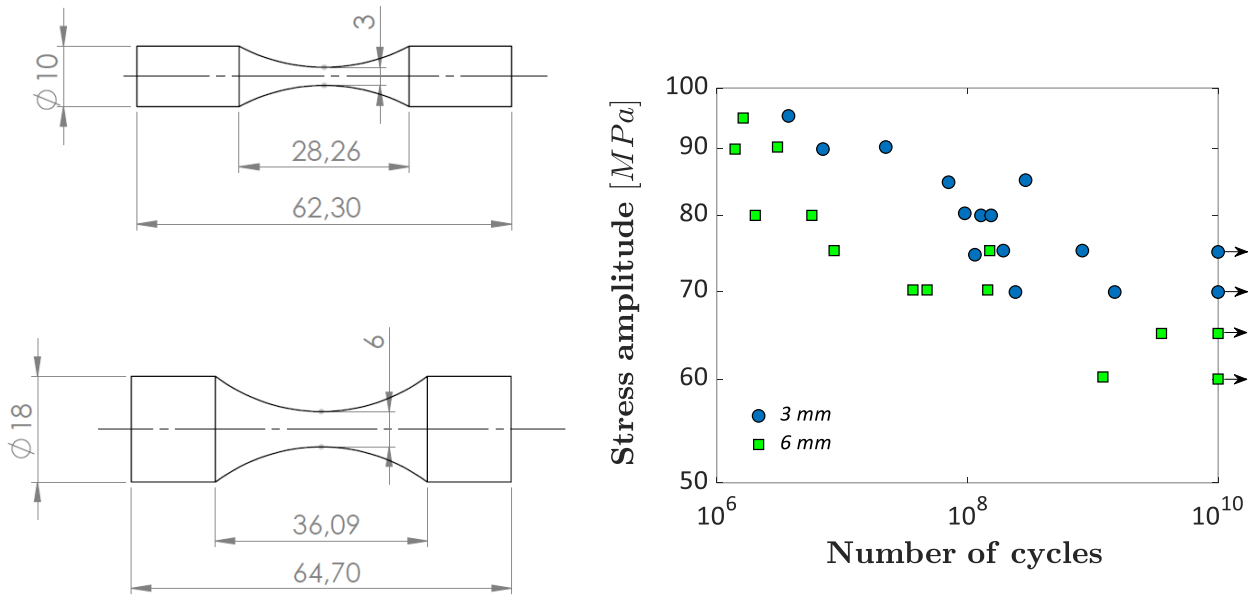

(a) (b)

Figure 15: Experimental tests in [46]: a) hourglass specimen geometries (not in scale); b) Experimental data on an S-N plot.

According to Fig. 15, the large scatter of experimental failures partially hides the influence of the specimen diameter on the VHCF response and some data for 3 mm and 6 mm gage diameter specimens partially overlap at stress amplitudes below $5 \cdot 10^8$ cycles. The difference is more evident for large number of cycles. For example, if the runout number of cycles is considered, the difference is evident, with the smallest stress amplitude at the runout N_f of 70 MPa for the 3 mm diameter hourglass specimens and of 60 MPa for the 6 mm diameter hourglass specimens. The Authors also investigated the fracture surfaces, with almost all the fatigue failures originating from pores with large size. A LEVD was assumed for the defect size: the critical defect sizes for the 3 mm were all below 400 μm, whereas for the 6 mm diameter specimens 4 specimens failed due to defects with sizes larger than 400 μm. According to the Authors, the average defect size increases from 338 μm for the 3 mm diameter to 361 μm for the 6 mm diameter. The Authors, moreover, proposed a model to estimate the P-S-N curves, by applying the weakest-link principle and by considering the probability of failure in each infinitesimal volume subjected to an almost constant stress amplitude. However, this model is not applied to the experimental data and a Weibull model is used for the fatigue life. A "size effect correction" factor for specimens characterized by different sizes was also proposed. The ratio between the fatigue strength obtained by testing specimens with larger diameter and volume, $s_{a,1}$, and

specimens with smaller diameter and volume, $s_{a,2}$ (the subscripts 1 and 2 refer to the large and the small specimen, respectively) is given by:

$$\frac{s_{a,1}}{s_{a,2}} = \left(\frac{\int_{-x_1}^{x_2} [G_2(x)]^{K\sigma} \cdot S_2(x) \cdot dx}{\int_{-x_1}^{x_2} [G_1(x)]^{K\sigma} \cdot S_1(x) \cdot dx} \right)^{\frac{1}{K\sigma}}, \tag{13}$$

where x is the longitudinal coordinate, with the origin at the specimen center, $G_1(x)$ and $G_2(x)$ Gaussian functions modelling the stress variation along the x axis, $S_1(x)$ and $S_2(x)$ the cross section-areas and K_σ a parameter to be estimated from experimental data. According to Eq. 13, size-effect is modelled by considering the stress variation and the specimen cross-section, without taking into account the distribution of defect size.

The experimental data, qualitatively digitized from the original paper by using the software Engauge, the "modified data" (experimental data obtained by testing $3\,\mathrm{mm}$ diameter specimens and shifted to the corresponding data at $6\,\mathrm{mm}$ diameter with Eq. 13) and the P-S-N curves estimated by considering the experimental results and the modified data (median, 0.1-th and 0.9-th quantiles) are plotted in Fig. 16. In Fig. 16, "mod" refers to the "modified data" and to the P-S-N curve estimated by considering the modified data. According to the Authors, the P-S-N curves estimated with the modified data are close to the experimental P-S-N curves, confirming the effectiveness of the proposed correction factor.

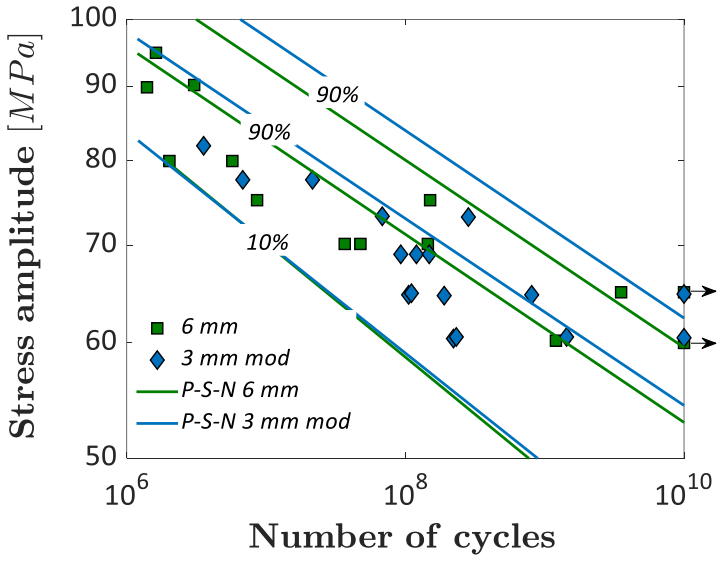

Figure 16: Experimental tests in [46]: experimental P-S-N curve and P-S-N curves estimated by considering the correction factor in Eq. 13.

In [47], size-effect is investigated by testing hourglass and dog-bone specimens with different diameters. Ultrasonic fully reversed tests were carried out on a low carbon steel. Figure 17 shows the geometry of the specimens tested and the experimental results. In particular, Figs. 17a, 17c and 17e show the geometries of

the tested specimens, whereas Figs. 17b, 17d and 17f show the experimental data in an S-N plot. For the sake of clarity, Fig. 17b shows the S-N plot of the experimental data obtained by testing the hourglass and the dog-bone specimens with the geometry in Fig 17a. Figure 17d shows the S-N plot of the experimental data obtained by testing the hourglass specimens with the geometry in Fig 17c. Figure 17f shows the S-N plot of the experimental data obtained by testing the hourglass specimens with the geometry in Fig 17e. According to Figs. 17a, 17c, and 17e the Authors focused on the effect of the specimen size, rather than on the effect of the specimen volume. It is worth noting that thin plate and hourglass specimens were also tested, but the results were mainly concentrated in the HCF region and, accordingly, they have not been considered. In the original paper hourglass specimens are called “sandglass” specimens; however, to be consistent with the nomenclature used in the present paper, they will be called “hourglass” specimens.

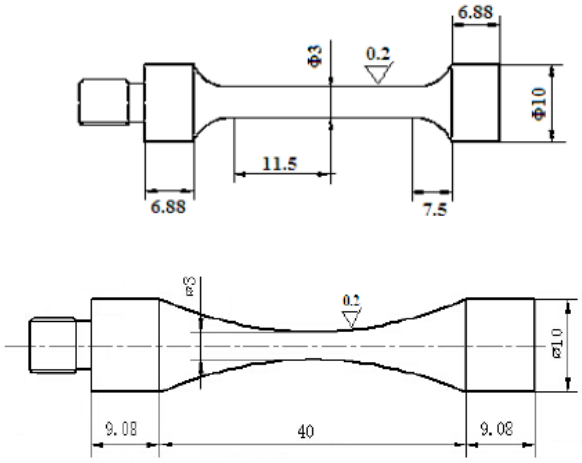

(a)

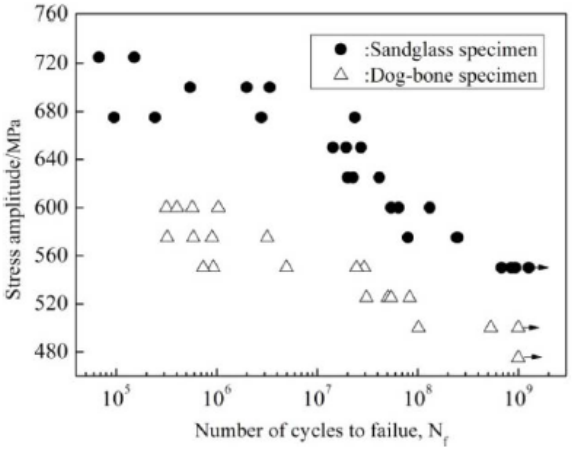

(b)

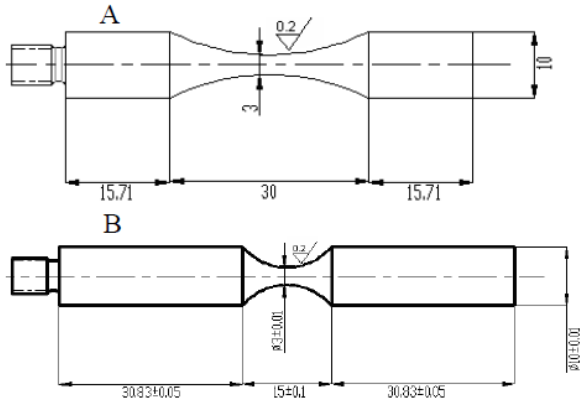

(c)

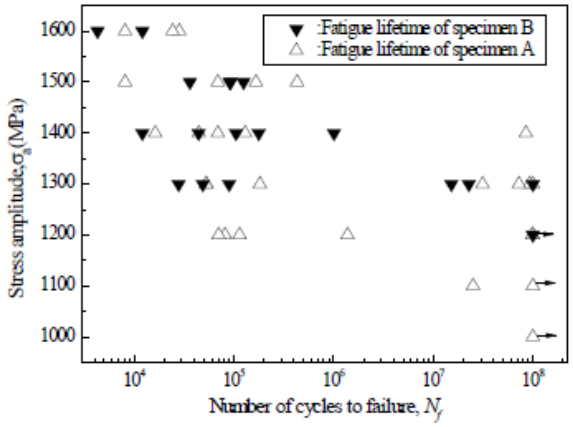

(d)

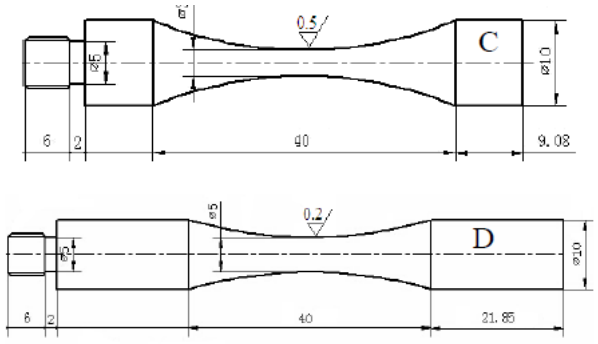

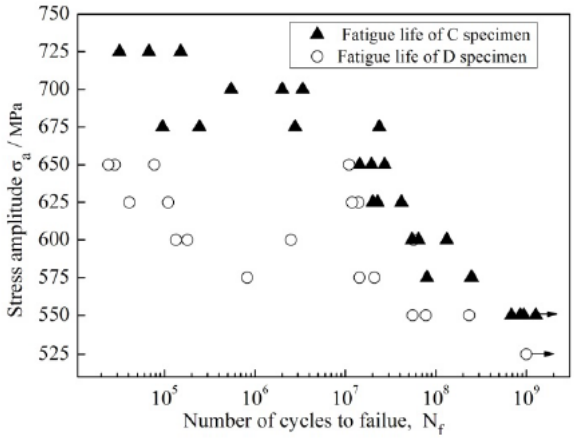

(e) (f)

Figure 17: Experimental tests in [47]: a) geometry of the specimens and b) S-N plot of the experimental data; c) geometry of the specimens and d) S-N plot of the experimental data; e) geometry of the specimens and f) S-N plot of the experimental data.

According to Fig. 17a and 17b, the specimen size significantly affects the VHCF response, with the experimental data for the hourglass specimens above the experimental data for the dog-bone specimens (at 10^9 cycles the smallest runout stress amplitude was equal to $540\ \mathrm{MPa}$ for the hourglass specimens, whereas it is equal to $480\ \mathrm{MPa}$ for the dog-bone specimens), with a 13% reduction. However, rather than the specimen size and type or the specimen diameter, which is the same, the VHCF decrement can be mainly attributed to the different tested V_{90}: indeed the V_{90} of the dog-bone and of the hourglass specimens, computed by the authors through FEA, was equal to $94\ \mathrm{mm}^3$ and to $42\ \mathrm{mm}^3$, respectively. Accordingly, dog-bone specimens characterized by larger V_{90} showed a smaller VHCF strength.

On the other hand, according to Figs. 17c and 17d, the experimental data obtained by testing hourglass specimens with the same gage diameter ($3\ \mathrm{mm}$) but with different geometries, are close each other with limited differences and a large scatter in the finite fatigue life range. However, the data for the finite fatigue life are mainly concentrated at N_f smaller than 10^6 cycles. If the data above 10^7 cycles are considered and, in particular, the runout stress amplitude, type A hourglass specimens show a larger VHCF strength (at 10^8 cycles the smallest runout stress amplitude was equal to $1200\ \mathrm{MPa}$ for the type B hourglass specimens, whereas it was equal to $1000\ \mathrm{MPa}$ for the type A hourglass specimens, with a 17% difference). Even in this case, the difference is mainly due to the different tested V_{90}, being equal to $30\ \mathrm{mm}^3$ for specimens A and to $9\ \mathrm{mm}^3$ for specimens B. The large difference above 10^7 cycles can be justified by considering that the risk-volume effect is larger at larger N_f, where the influence of defect plays a more significant role. It must be also noted that in specimens B the stress concentration factor is larger (about 1.134) than that of specimen A (about 1.04, according to [19]). Therefore, size-effect is partially hidden by the stress concentration in specimens B, that could have lowered the VHCF response and contributed to the large scatter.

The experimental datapoints shown in the S-N plot in Fig. 17f were obtained by testing hourglass specimens with different gage diameter, $3\ \mathrm{mm}$ for specimen C and $5\ \mathrm{mm}$ for specimen D (Fig. 17e). According to Fig. 17f, the data for the hourglass specimens with $3\ \mathrm{mm}$ diameter are above the data for the specimens with $5\ \mathrm{mm}$ diameter, with a 5% difference at 10^9 cycles (from $550\ \mathrm{MPa}$ to $525\ \mathrm{MPa}$). Differently from the other cases, where the gage diameter is the same, for hourglass C and D the diameter was different, with the hourglass specimens characterized by the smallest diameter being above the data for the hourglass specimens with $5\ \mathrm{mm}$ diameter. Also in this case, as the risk-volume increases ($V_{90} = 30\ \mathrm{mm}^3$ for specimen C and $V_{90} = 170\ \mathrm{mm}^3$), the VHCF strength decreases. According to the results in [47], the volume, rather than the diameter, seems to be more relevant for assessing size-effects in VHCF. Indeed, specimens with the same gage diameter were characterized by different VHCF strengths, pointing out that the different V_{90} can be only considered to justify this difference. If the diameter had been the most significant influencing factor, specimens with the same diameter should have been characterized by the same VHCF strength.

In [15, 16], a different approach is followed to deal with size-effect in VHCF. In particular, size-effect is modelled with "*Fractal Geometry concepts*" in order to assess scale-independent P-S-N curves. The concept of fractality is applied to provide a theoretical explanation for the dependency between the specimen size and the VHCF response. The disorder induced by defects is modelled by assuming that the reacting section, or ligament, of the material is a lacunar fractal set with non-integer dimension [16]. By considering the Weibull distribution, the expression for the probabilistic stress-life relation is given by:

$$\log_{10} N_f = \bar{\beta} \cdot [-\ln(1-P)]^{\bar{\alpha}} \left(\frac{\Delta\sigma_{0,50\%}}{\Delta s}\right)^n, \tag{14}$$

where P is the probability of failure, Δs the applied stress range, $\bar{\alpha}$, $\bar{\beta}$ the two parameters of the Weibull distribution, $\Delta\sigma_{0,50\%}$ and n the best fitting parameters of the median curve S-N curve. In order to introduce the fractal concept, the following scaling law has been assumed for the stress range:

$$\Delta s = \Delta s^* \cdot b^{-d_\sigma}, \tag{15}$$

where Δs^* is the fractal stress range, b the characteristic specimen size and d_σ is the decrement of the ligament due to the presence of defects. A similar scaling law was assumed for the term $\Delta\sigma_{0,50\%}$:

$$\Delta\sigma_{0,50\%} = \Delta\sigma^*{}_{0,50\%} \cdot b^{-d_\sigma}, \tag{16}$$

According to the Authors, by substituting Eq. 15 in Eq. 14, the P-S-N curves as a function of the specimen size b can be obtained. On the other hand, if Eq. 16 is substituted in Eq. 14, the P-S-N curves obtained by testing

specimens with different sizes can be collapsed in into a unique fractal specimen-size independent P-S*-N curve.

The proposed approach has been validated through an experimental dataset obtained by the Authors with ultrasonic fully reversed tension-compression tests on specimens made of EN-AW6082 Aluminium alloy. Hourglass specimens with $3\ \mathrm{mm}$, $6\ \mathrm{mm}$ and $12\ \mathrm{mm}$ diameters were tested. The specimen geometry is shown in Fig. 18 a ($3\ \mathrm{mm}$ and $6\ \mathrm{mm}$ hourglass specimens) and 18b ($12\ \mathrm{mm}$ hourglass specimens). The size-dependent P-S-N curves are shown in Fig. 18c, whereas all the data collapsed in one curve are shown in Fig. 18 d.

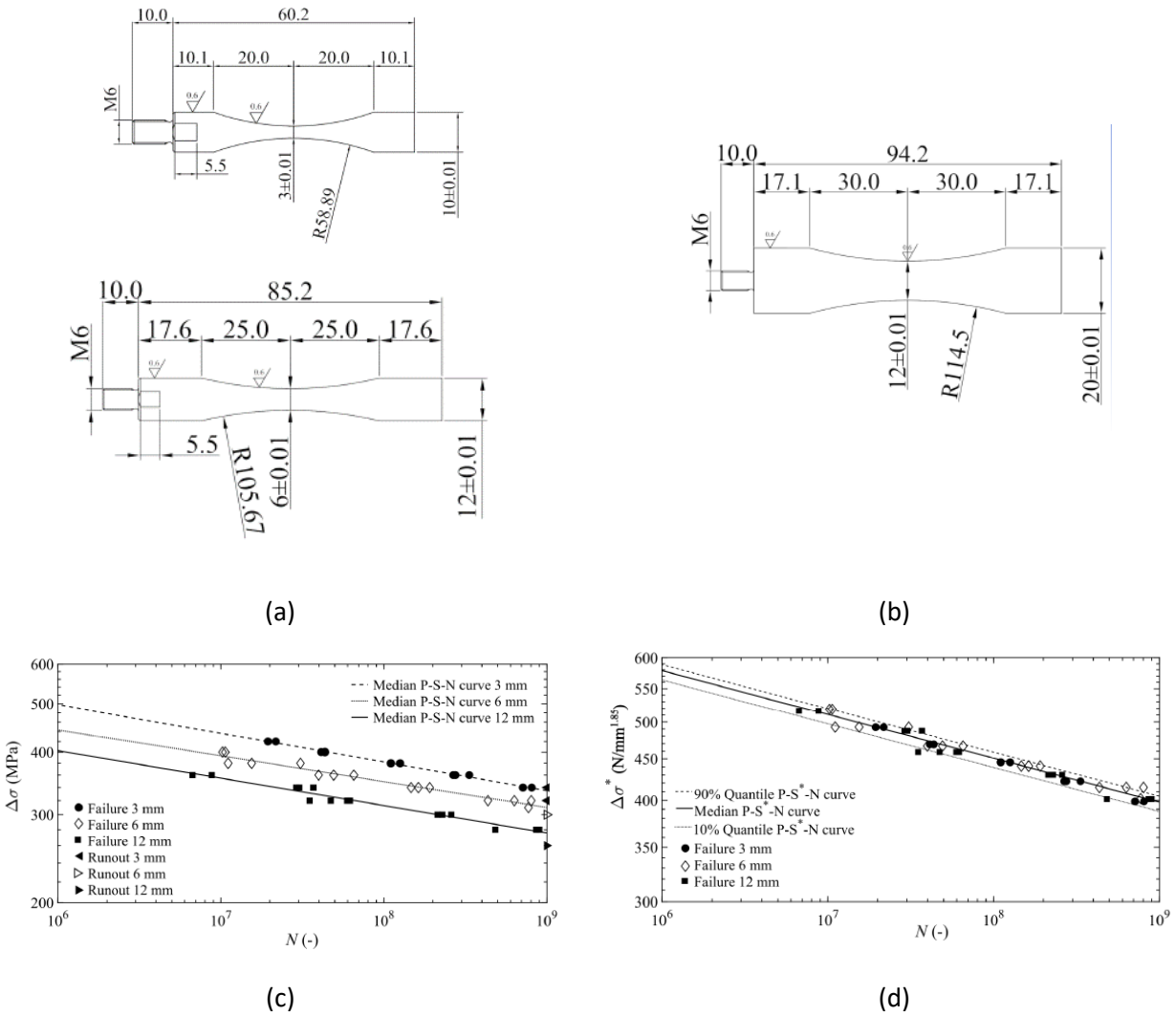

Figure 18: Experimental tests in [16]: a) geometry of the $3\ mm$ and $6\ mm$ hourglass specimens; b) geometry of the $12\ mm$ hourglass specimens c) size-dependent P-S-N curves; d) specimen-size independent P-S*-N curve.

According to Fig. 18c, the proposed model permits to assess the dependency between the fatigue strength and the specimen size. The median S-N curves shift downward with the diameter. The stress amplitude decrement at 10^9 cycles is equal to $13\ \mathrm{MPa}$ from $3\ \mathrm{mm}$ to $6\ \mathrm{mm}$ (8% decrement), whereas it is equal to

$18\,\mathrm{MPa}$ from $6\,\mathrm{mm}$ to $12\,\mathrm{mm}$ (12% decrement). Size-effect therefore increases with the specimen diameter, differently from [45], where size-effect seems to approach an asymptotic trend above $6\,\mathrm{mm}$ diameter. However, size-effect has been only estimated in [45], without any experimental investigation. The collapsed P-S*-N curves, moreover, properly fit the experimental data, with almost all the experimental failures within the 0.1-th quantile and the 0.9-th quantile of the P-S-N curves.

3. DESIGN METHODOLOGIES AND DISCUSSION

In Section 3.1 the design methodologies developed in the literature for taking into account size-effects in VHCF are analyzed. In Section 3.2 the experimental results on size-effect in VHCF are discussed, focusing on the strengths and on the weak points of the available results and on the objectives of the future research.

3.1 VHCF design and size-effect

In this Section, the procedures developed for the design of components subjected to VHCF loads are analysed. According to [22], the prediction of the largest defects with the LEVD, Eq. 3, is not sufficient to ensure a safe design of components against VHCF failures. For example, when the crack starts propagating from the ODA in VHCF, the ODA size in place of the defect size should be considered for the application of the Murakami formulation. Indeed, the crack does not start propagating from the initial defect, but from the border of the ODA (i.e., the SIF equals the SIF threshold at the ODA border, and not at the defect border). Accordingly, the Murakami formulation applied by considering the defect size in place of the ODA size provides a non-conservative estimation of the fatigue limit, according to [22].

In [22], a procedure for the design of components that takes into account the crack nucleation from defects with ODA formation is proposed. Figure 19 shows the flow charts of the proposed methodology. The procedure involves fatigue tests on specimens made with the component material, in order to assess the so-called *Master curves of ODA*, which model the dependency between the ratio $\sqrt{area_{ODA}}/\sqrt{area_{max}}$ and N_f. $area_{ODA}$ is the area of the ODA, whereas $area_{max}$ is the area of the largest inclusion expected to occur (in the specimen or in the component volume). The *Master curves of ODA* are obtained by fitting the experimental data on the $\sqrt{area_{ODA}}/\sqrt{area_{max}}$ - N_f plot.

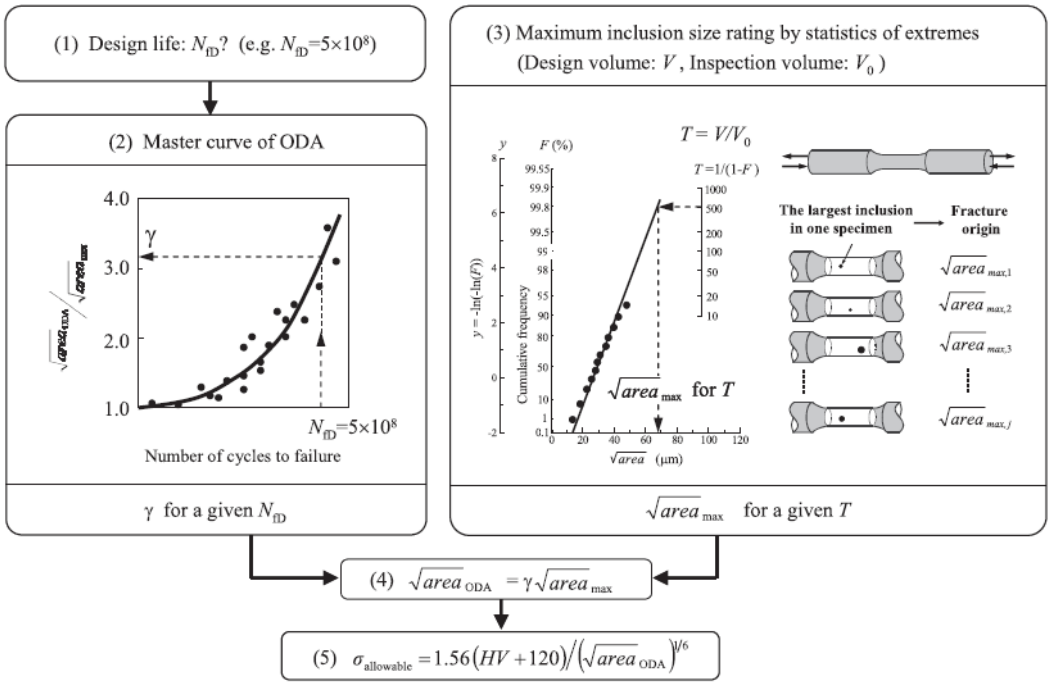

Figure 19: Procedure for the design against VHCF failures that takes into account size-effect in [22].

According to Fig. 19, at first the fatigue life to be considered for the design, N_D, should be defined (step 1). Given N_D, the parameter $\gamma = \sqrt{area_{ODA}}/\sqrt{area_{max}}$ can be obtained from the *Master curves of ODA*. Thereafter, from the LEVD associated to the defect size (with parameters estimated from the defects measured on the fracture surfaces or through inclusion sampling), $\sqrt{area_{max}}$ for the design volume V is assessed (in Fig. 19, V_0 is the "inspection volume", i.e., the volume considered for the estimation of the LEVD parameters). Given γ and $\sqrt{area_{max}}$ the size of the ODA in the component volume can be easily computed as $\sqrt{area_{ODA}} = \gamma \cdot \sqrt{a_{d,0}}_{max}$. Finally, according to step 5 (Fig. 19), the fatigue limit for the design N_D can be computed by applying the Murakami formulation and by considering the estimated $\sqrt{area_{ODA}}$. The procedure, which requires that the *Master curves of ODA* are properly estimated, has been also applied for the design of a component made of a JIS-SCM435 steel ($HV = 600$) [22]. N_D was chosen equal to $5 \cdot 10^8$ cycles and $V = 100000\, mm^3$. The estimated fatigue limit was equal to $441\, MPa$. On the contrary, if $\sqrt{area_{max}}$ in place of $\sqrt{area_{ODA}}$ had been considered, the fatigue strength would have increased to $546\, MPa$, with a 24% non-conservative difference. This design methodology pointed out the importance of taking into account the ODA size if the mechanisms of crack initiation involve the ODA formation.

In [32], a method for the design against VHCF failures based on FEA and on the weakest-link approach is proposed. The model was validated on HCF data, but the Authors pointed out that VHCF response can be safely extrapolated from HCF data with negligible errors. The Authors proposed a methodology for assessing the effective volume, V^*_{eff}, which can be exploited for the design of components. The procedure for the estimation of the effective volume has been analyzed in Section 2.2 and will not be recalled for the sake of

brevity. V_{eff}^{*} can be computed for each element of the FE model of the component that has to be designed. Given V_{eff}^{*}, the failure stress for each element can be obtained. The procedure proposed by the Authors involves verifying if the stress level computed through FEA at each integration point is below the failure stress. If all the elements are characterized by a stress level below the failure stress, the component does not fail.

In [39], a procedure for the design against VHCF failures based on the *fatigue limit design curves* is proposed. The *fatigue limit design curves* provide the variation of the fatigue limit with respect to the V_{90}, according to Eq. 6. As for the methodology in [22], the influence of the FGA size on the crack nucleation is taken into account, since the parameters for the fatigue limit design curves are estimated by considering the FGA size. Therefore, the proposed procedure can be applied only if the FGA sizes are properly measured on the fracture surface. Fig. 20 shows the design procedure developed in [39].

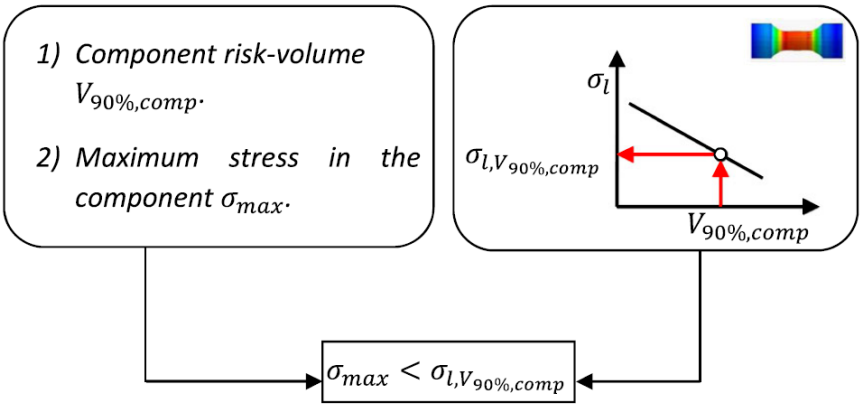

Figure 20: Procedure for the design against VHCF failures that takes into account size-effect in [39].

According to Fig. 20, the procedure defined in [39] involves three steps. The first one (rectangle on the left) involves an FEA of the component in order to assess the component risk-volume, $V_{90\%,comp}$, and the largest stress within the component, σ_{max}. Concurrently, the fatigue limit for the $V_{90\%,comp}$ can be easily obtained ($\sigma_{l,V_{90\%,comp}}$) by considering the relation between the fatigue limit and the V_{90}, estimated from the experimental results according to the model reported in Eq. 8. The component is verified if σ_{max} is smaller than $\sigma_{l,V_{90\%,comp}}$. It can be noted that the proposed procedure can be applied also for a specific N_f, by considering the relation reported in Eq. 9 and applied in [31]: in this case, the P-S-N curves for the component volume can be predicted from the P-S-N curves estimated by considering the experimental data. Given the P-S-N curves for the component volume, the limit stress amplitude can be assessed by considering the selected N_f and is equal to $\sigma_{l,N_{f,comp}}$. The component is verified if $\sigma_{max} < \sigma_{l,N_{f,comp}}$. In both cases, high reliability quantiles should be considered for the estimation of $\sigma_{l,V_{90\%,comp}}$ and $\sigma_{l,N_{f,comp}}$, in order to take into account the possible large scatter associated to the experimental data.

This analysis pointed out that the available design procedures can be applied only if the VHCF response for the component material is experimentally assessed and, furthermore, the importance of investigating the failure origin, in order to assess the defect size distribution and the FGA/ODA size associated to each failure.

3.2 Discussion

In this Section, the experimental results on size-effects in VHCF are analyzed and discussed. Figure 21 shows the percentage VHCF strength decrement with respect the risk-volume V_{90}. For each investigated material, the VHCF strength is normalized with respect to the VHCF strength of the specimens with the smallest V_{90}. Accordingly, the normalized VHCF strength of the specimens with the smallest V_{90} is equal to 100%. The variation corresponds to that reported in the original paper; if not available, the VHCF strength at the runout number of cycles has been retrieved through digitization of the S-N plots reported in the original paper. For the sake of clarity, Fig. 21a shows the experimental results obtained by testing specimens with the largest V_{90} smaller than $200\ mm^3$. Figure 21b shows the experimental results obtained by testing specimens with the largest V_{90} smaller than $3000\ mm^3$. Figure 21c shows the experimental results obtained by testing specimens with the largest V_{90} larger than $3000\ mm^3$.

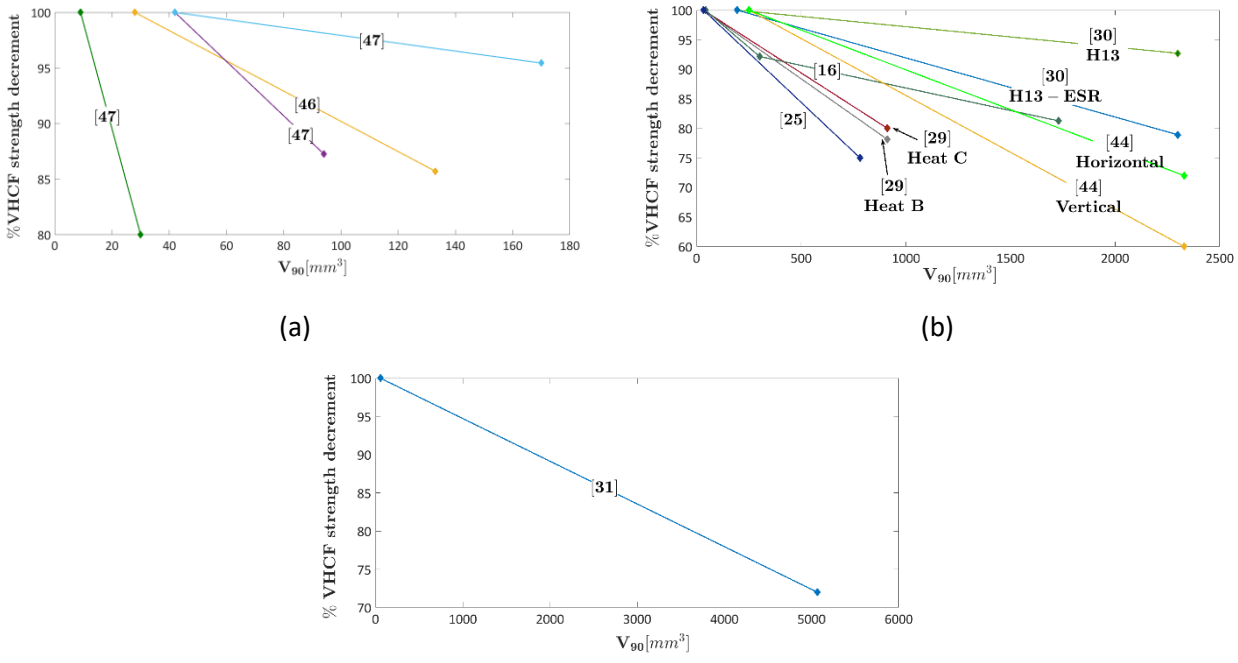

(a) (b)

(c)

Figure 21: VHCF strength percentage variation (normalized by the VHCF strength of the smallest tested V_{90} in each analyzed paper) with respect to the tested V_{90}; a) largest V_{90} smaller than $200\ mm^3$; b) largest V_{90} smaller than $3000\ mm^3$; b) largest V_{90} smaller than $5000\ mm^3$.

According to Fig. 21, size-effect significantly affects the VHCF response. However, differently from the HCF response, a general rule can be hardly extrapolated from the experimental data. Indeed, the VHCF decrement depends not only on the tested risk-volume, but on the material, on the manufacturing process and on the defect size range, or better on the material sensitivity to the increment of defect size with the risk-volume. The VHCF strength variation for the H13 steel and the AlSi10Mg, experimentally investigated through tests on specimens with the same V_{90}, is 21% for the unrefined H13, 7% for the refined H13 ESR steel and is significantly larger for the AlSi10Mg specimens [28%-40%]. These results point out the dependency of size-effects on the material type and on the material cleanliness. On the other hand, by testing specimens with smaller risk-volume increment [25, 29], the decrement is similar to that found in [30], further suggesting a material dependency. It is worth noting that the scatter associated with the experimental data, due to the randomness of the defect size, can affect the computation of the VHCF strength decrement. For example, for tests on AlSi10Mg vertical specimens in [44], the decrement is equal to 17% by considering the median VHCF strength and increases to 40% by considering the 0.001-th quantile curve. This highlights an important aspect: the experimental scatter associated to size-effect has been rarely investigated and taken into account in the literature, even if the randomness associated to the defect size and intrinsically associated to the fatigue phenomenon should be carefully taken into account, especially if the primary objective is the design of components.

These results confirmed that the material type and manufacturing process, the defect size range (or defect sensitivity to material volume increment) and the material cleanliness strongly influence size-effect, highlighting the importance of properly estimating the defect size distribution and experimentally verifying size-effect through tests on specimens with large risk-volumes. In this respect, the validity of tests on specimens with small risk-volumes should be discussed. For example, in [29], different inclusion types were found, and the TiN inclusion were found only in small specimens, suggesting a size-effect associated to the defect type. If the defects found through tests on small risk-volume follow a LEVD different from that of defects present in large volumes typical of components, the prediction of the largest defect based on tests on small specimens may be non-conservative, with large differences. In this case, tests on specimens with large risk-volumes are suggested in order to properly assess the defect population and the size distribution in the component volume. On the other hand, if the defect type does not vary with the risk-volume, tests on small specimens may permit to properly predict the largest defect and can be used for the design of components. Even in this case, however, tests on specimens with different risk-volumes are recommended, according to [39].

As discussed in Section 2.2, the choice of the proper volume at risk for the application of the LEVD is fundamental, but its definition is not unique. The use of the V_{90} proved to be a reasonable and effective choice in many cases and permits for a rapid assessment of the volume at risk and of the largest defect. However, the definition of the volume at risk, especially for components with complex shapes (like those

produced with AM processes), should be more reliably assessed by considering the defect size, the stress distribution and the defect location [34]. On the other hand, these methodologies would involve a FE analysis and a more complex parameter estimation.

Moreover, all the analyses on size-effects in VHCF assume that the factors affecting the crack nucleation in VHCF from defects do not depend on the defect size. However, this should be experimentally verified. For example, if the VHCF crack originates with hydrogen assistance and with ODA formation, is the hydrogen contribution dependent on the defect size? Are large defects characterized by larger trapping sites and higher hydrogen concentrations that can affect the crack nucleation process? If grain refinement occurs, is this mechanism of crack nucleation defect size sensitive? The dependency between factors affecting the crack nucleation processes in VHCF and the defect size should be investigated, in order to fully understand size-effects in VHCF. Indeed, if the crack nucleation process depends on the defect size, models for size-effects must take into account this contribution.

Size-effect has been mainly investigated by considering the influence of the risk-volume. In the last years, methodologies based on the influence of the specimen size, or of the specimen diameter or cross-section have been proposed and proved to be effective, especially when information on the defect originating cracks is not available. In particular, in [16], the methodology has been experimentally validated by considering three specimen sizes. The strategy of condensing all the data in a unique curve could represent an efficient solution for the design of components. However, the experimental results obtained in [47] seems to demonstrate that the risk-volume is the most influencing parameter, since specimens with the same cross-section and different V_{90} are characterized by different VHCF strengths. However, both the risk-volume and the diameter dependency should be analyzed, and more experimental tests should be carried out to assess which is the most influencing parameter.

It must be noted that tests on specimens with different diameters were carried out in [48]. The Authors analyzed the crack nucleation process, highlighting that it is the same and does not depend on the specimen size. The Authors, therefore, justified the different VHCF strengths with the largest temperature increment in specimens with larger diameters. The temperature increment in ultrasonic tests could be limited by using appropriate cooling systems or through intermittent tests [18, 49], even in specimens with large cross-sections [50]. Moreover, the randomness distribution of critical defects in specimens with large V_{90} and gage diameter suggests that the temperature distribution is almost uniform even in large specimens. In addition, in [47] specimens with the same diameter but characterized by different V_{90} were tested, and the VHCF strength of specimens with small V_{90} was larger than that of large specimens. Therefore, a temperature dependency can be excluded, with the different VHCF strength caused by the different tested V_{90}.

To conclude, size-effect is an important factor to deal with when analyzing the VHCF response of materials, since it has significant implications when components are to be designed. More efforts should be done to

assess all the factors affecting size-effect, in order to provide high-reliability design methodologies against VHCF failures.

4. CONCLUSIONS

In this paper, the influence of size-effect on the VHCF response has been critically reviewed, by analyzing the experimental literature results obtained by testing specimens with different sizes. Moreover, the methodologies proposed for modelling size-effect in VHCF fatigue and the design procedures currently available have been described and discussed. The following conclusions can be drawn:

1) Size-effect in VHCF is generally modeled by considering the statistical dependency of the defect size with the highly stressed material volume, the so-called "risk-volume". However, a unique definition for the risk-volume is not available in the literature. The V_{90} (volume of material subjected to a stress amplitude larger than the 90% of the maximum applied stress) proved effective in modeling the volume at risk. However, the V_{90} fails to account the stress gradient and the stress distribution within the material volume. Accordingly, statistical methodologies for the analysis of size-effect that do not require an a priori definition of the risk-volume and that models the stress distribution and the stress gradient within the part volume have been also proposed and validated.
2) A strong dependency between size-effect, fatigue limit and the VHCF strength in the finite fatigue life range has been found experimentally. The dependency is mainly related to the increment of the defect size within the risk-volume. The variation of the fatigue limit, i.e., the threshold for crack propagation, with respect to the defect size has been modeled in the literature by exploiting the properties of the Largest Extreme Value distribution. For steels, the decrement of the VHCF limit was found to be above 30% from the lab specimens to real components. The capability of predicting the VHCF limit starting from tests on small specimens was also verified, showing that the steel cleanliness plays an important role in size-effect. Indeed, the VHCF limit can be more reliably predicted for steels characterized by a high degree of purity.
3) The risk-volume was also found to significantly affect the finite VHCF life range. Even in this case, the dependency is related to the increment of defect size with the risk-volume. Experimental tests were carried out in the literature on high strength steels and on Aluminum alloy specimens with a minimum V_{90} equal to $33\ \mathrm{mm}^3$ and a maximum tested V_{90} equal to $5000\ \mathrm{mm}^3$. A significant decrement of the VHCF strength with the risk-volume was experimentally found, up to 40%. The VHCF decrement intensity was found to depend on the material type, material cleanliness and manufacturing process. Therefore, size-effect in the finite VHCF life cannot be assessed only by considering risk-volume variation, but the material type, the material

defectiveness and the production process should be also carefully considered. A general rule for size-effect on the VHCF strength could not be found in this research, and more experimental results are necessary to clarify the influence of the above-mentioned factors.

4) The specimen diameter or the specimen cross-section also influence the VHCF response. Experimental tests on steel and Aluminium alloy specimens have been carried on hourglass and dog-bone specimens with diameters from $3\ \mathrm{mm}$ to $12\ \mathrm{mm}$. The VHCF strength was found to decrease with the specimen diameter, with decrements up to 20%. In order to model the dependency between the VHCF strength and the specimen diameter, the fractal approach has been used. In particular, a procedure for collapsing the experimental data obtained by testing specimens with different sizes in a unique fractal specimen-size independent P-S-N curve has been proposed and validated, proving the effectiveness of this alternative approach. However, it was also experimentally found that the VHCF strength decreases in specimens with the same cross-section but different risk-volumes. In this case, the VHCF strength decrement can be only ascribed to the different tested risk-volumes, proving that a physical-based approach that considers the risk-volume as the most influencing factor is more effective to model size-effect. More experimental tests are necessary to assess if approaches based on risk-volume and specimen cross-section must be considered together to properly model size-effect.

5) The design procedures available in the literature for preventing VHCF failures of components have shown the importance of taking into account the Optically Dark Area (ODA) size and not only the defect size. Otherwise, the limit stress cannot be conservatively assessed, thus affecting the structural integrity of the designed component.

6) All the analyses on size-effect in VHCF are based on the assumption that the factors affecting the crack nucleation in VHCF from defects do not depend on the defect size. However, this aspect should be experimentally verified, since it could help explaining and fully understanding size-effect in VHCF.

7) Tests on specimens with large risk-volumes are recommended. Indeed, the defect population could vary with the risk-volume. In this case, the defect size distribution assessed through tests on specimens with small volumes could be different from that of components with large volumes. Therefore, the defect size may not be properly predicted by considering the results of tests on small volumes.

8) A general rule for size-effect in VHCF has not been proposed yet. However, the experimental results suggest that material type, manufacturing process, heat treatment, cleanliness and defect size range (or defect sensitivity to material volume) strongly influence size-effect in VHCF.

The analyses carried out in this paper highlight the importance of experimentally verifying size-effect in VHCF. More effort should be made to fully understand and model this complex phenomenon, since it has significant implications on the design of components and could affect their structural integrity.

ACKNOWLEDGMENTS

The research leading to these results has received funding from the European Union's Horizon 2020 innovation action program under grant agreement No 101006844 –Fatigue4Light project.

REFERENCES

1 Weibull W. A statistical theory for the strength of materials. Stock-holm: Swedish Royal Institute for Engineering Research; 1939.

2 Bažant ZP. Size effect in blunt fracture: concrete, rock, metal. Journal of Engineering Mechanics. 1984; 110: 518-535.

3 Lei W-S, Qian G, Yu Z, Berto F. Statistical size scaling of compressive strength of quasi-brittle materials incorporating specimen length-to-diameter ratio effect. Theoretical and Applied Fracture Mechanics. 2019; 104: 102345.

4 Qian G, Wei-Sheng L. (2019) A statistical model of fatigue failure incorporating effects of specimen size and load amplitude on fatigue life, Philosophical Magazine, 99:17, 2089-2125, DOI: 10.1080/14786435.2019.1609707

5 M. Shirani, G. Härkegård, Fatigue life distribution and size effect in ductile cast iron for wind turbine components, Engineering Failure Analysis, Volume 18, Issue 1, 2011, Pages 12-24, ISSN 1350-6307, https://doi.org/10.1016/j.engfailanal.2010.07.001.

6 M. Muniz-Calvente, A.M.P de Jesus, J.A.F.O. Correia, A. Fernández-Canteli, A methodology for probabilistic prediction of fatigue crack initiation taking into account the scale effect, Engineering Fracture Mechanics, Volume 185, 2017, Pages 101-113, ISSN 0013-7944, https://doi.org/10.1016/j.engfracmech.2017.04.014.

7 Li Lee, Y., Pan, J., Hathaway, R. and Barkey, M. (2005) Fatigue Testing and Analysis: Theory and Practice, Elsevier Butterworth- Heinemann: New York (USA).

8. Murakami Y. Metal Fatigue: Effects of Small Defects and Nonmetallic Inclusions. Oxford, UK: Elsevier Ltd; 2002.

9 Samuel Kœchlin, FKM Guideline: Strengths, Limitations and Experimental Validation, Procedia Engineering, Volume 133, 2015, Pages 309-319, ISSN 1877-7058, https://doi.org/10.1016/j.proeng.2015.12.674.

10. Sippel JP, Kerscher E. Properties of the Fine Granular Area and Postulated Models for Its Formation during Very High Cycle Fatigue—A Review. *Appl. Sci.* 2020; 10: 1-27.

11. Murakami Y, Nomoto T; Ueda T. Factors influencing the mechanism of superlong fatigue failure in steels. *Fatigue Fract. Eng. Mater. Struct.* 1999; 22: 581–590.

12. Sakai T, Harada H, Oguma N. Crack initiation mechanism of bearing steel in very high cycle fatigue. In Proceedings of the ECF, Alexandroupolis, Greece, 3–7 July 2006; p. 16.

13. Sakai T; Sato Y, Oguma N. Characteristic S-N properties of high-carbon-chromium-bearing steel under axial loading in long-life fatigue. *Fatigue Fract. Eng. Mater. Struct.* 2002; 25: 765–773.

14. Shiozawa K, Morii Y, Nishino S. Subsurface Crack Initiation and Propagation Mechanism under the Super-Long Fatigue Regime for High Speed Tool Steel (JIS SKH51) by Fracture Surface Topographic Analysis. *JSME Int. J*. 2006; 49: 1–10.

15 Carpinteri, A.; Montagnoli, F.; Invernizzi, S. Scaling and Fractality in Fatigue Resistance: Specimen-Size Effects on Wöhler's Curve and Fatigue Limit. Fatigue Fract. Eng. Mater. Struct. 2020, 43, 1869–1879

16 Invernizi AS Invernizzi, S.; Montagnoli, F.; Carpinteri, A. Experimental Evidence of Specimen-Size Effects on EN-AW6082 Aluminum Alloy in VHCF Regime. Appl. Sci. 2021, 11, 4272. https://doi.org/10.3390/app11094272

17. Bathias C, Paris PC. Gigacycle Fatigue in Mechanical Practice. New York, USA: CRC Dekker; 2005.

18 Stanzl-Tschegg S. Very high cycle fatigue measuring techniques. *Int J Fatigue*. 2014; 60:2-17.

19 Paolino, D. S., Tridello, A., Chiandussi, G. and Rossetto, M. (2014) On specimen design for size effect evaluation in ultrasonic gigacycle fatigue testing. Fatigue Fract. Engng. Mater. Struct., 37, 570–579.

20 Masuo M, Tanaka Y, Morokoshi Y, Yagura H, Uchida T, Yamamoto Y, Murakami Y. Influence of defects, surface roughness and HIP on the fatigue strength of Ti-6Al-4V manufactured by additive manufacturing. Int J Fatigue 2018; 117: 163-179. https://doi.org/10.1016/j.ijfatigue.2018.07.020

21. Chapetti MD, Tagawa T, Miyata T. Ultra-long cycle fatigue of high-strength carbon steels part II: Estimation of fatigue limit for failure from internal inclusions. *Mater Sci Eng A*. 2003; 356: 236–244.

22 Matsunaga H, Sun C, Hong Y, Murakami Y. Dominant factors for very-high-cycle fatigue of high-strength steels and a new design method for components. Fatigue Fract. Engng. Mater. Struct. 2015, 38, 1274–1284.

23 Tridello A, Paolino DS, Chiandussi G, Rossetto M. Comparison between dog-bone and Gaussian specimens for size effect evaluation in gigacycle fatigue. Frattura e Integrità Strutturale. 2013;26:49-56.

24 T. Sakai, B. Lian, M. Takeda, K. Shiozawa, N. Oguma, Y. Ochi, M. Nakajima, T. Nakamura, Statistical duplex S–N characteristics of high carbon chromium bearing steel in rotating bending in very high cycle regime, International Journal of Fatigue, Volume 32, Issue 3, 2010, Pages 497-504, https://doi.org/10.1016/j.ijfatigue.2009.08.001.

25 Y. Furuya, Specimen size effects on gigacycle fatigue properties of high-strength steel under ultrasonic fatigue testing. Scripta Materialia 58 (2008) 1014–1017.

26 Sanaei N, Fatemi A. Defects in additive manufactured metals and their effect on fatigue performance: A state-of-the-art review. *Progress in Materials Science*, (In press). https://doi.org/10.1016/j.pmatsci.2020.100724

27 Sanaei N, Fatemi A, Phan N. Defect characteristics and analysis of their variability in metal L-PBF additive manufacturing, *Mater Design* 2019; 182: 108091. https://doi.org/10.1016/j.matdes.2019.108091

28 Kolyshkin A, Grigorescu A, Kaufmann E, Zimmermann M, Christ HJ. Development of a probabilistic model for the prediction of fatigue life in the very high cycle fatigue (VHCF) range based on inclusion population. *Procedia Struct Integr*. 2016;2: 1085–1092.

29 Furuya Y. Notable size effects on very high cycle fatigue properties of high strength steel. Mater Sci Eng A. 2011;528:5234-5240.

30 Tridello A, VHCF Response of Two AISI H13 Steels: Effect of Manufacturing Process and Size-Effect. Metals 2019, 9, 133; doi:10.3390/met9020133

31 A. Tridello, D.S. Paolino, M. Rossetto. Ultrasonic VHCF Tests on Very Large Specimens with Risk-Volume Up to 5000 mm^3. Applied Sciences 2020, 10, 2210.

32. Chantier I, Bobet V, Billardon R, Hild F. A probabilistic approach to predict the very high-cycle fatigue behaviour of spheroidal graphite cast iron structures. *Fatigue Fract Eng Mater Struct*. 2000; 23: 173–180.

33 Tridello A, Paolino DS, Chiandussi G, Rossetto M VHCF strength decrement in large H13 steel specimens subjected to ESR process. Procedia Structural Integrity 2 (2016) 1117–1124.

34 Paolino DS. Very high cycle fatigue life and critical defect size: Modeling of statistical size effects. *Fatigue Fract Eng Mater Struct*. 2021; 44 (5): 1209-1224.

35 T. Abe, Y. Furuya, S. Matsuoka, 10^{10}-cycles fatigue properties for a series of SUP 7 spring steels Trans. JSME Ser. A 70–696 (2004) 1050.

36 Zhang JW, Lu LT, Wu PB, Ma JJ, Wang GG, Zhang WH. Inclusion size evaluation and fatigue strength analysis of 35CrMo alloy railway axle steel. Mater Sci Eng A. 2013; 562: 211-217.

38 Paolino DS, Tridello A, Chiandussi G, Rossetto M. Estimation of P-S-N curves in very-high-cycle fatigue: Statistical procedure based on a general crack growth rate model. *Fatigue Fract Eng Mater Struct.* 2018; 41: 718–726.

39 Tridello A, Paolino DS, Chiandussi G, Rossetto M. Effect of electroslag remelting on the VHCF response of an AISI H13 steel. Fatigue Fract. Eng. Mater. Struct. 2017; 40: 1783–1794.

40 Paolino DS, Tridello A, Chiandussi G, Rossetto M. S-N curves in the very-high-cycle fatigue regime: statistical modeling based on the hydrogen embrittlement consideration. *Fatigue Fract Eng Mater Struct.* 2016; 39.

41 Furuya Y, Size effects in gigacycle fatigue of high-strength steel under ultrasonic fatigue testing, Procedia Engineering 2010; 2 (1): 485-490. https://doi.org/10.1016/j.proeng.2010.03.052.

42 Sun C, Zhang X, Liu X, Hong Y. Effects of specimen size on fatigue life of metallic materials in high-cycle and very-high-cycle fatigue regimes. *Fatigue Fract Eng Mater Struct.* 2016; 39: 770–779.

43 Linhart V, Auředník A, Furbacher I, černý I, Zima R, Matušek P, Novosad M. Experimental modelling and evaluation of fatigue strength and damage mechanisms of railway axles and wheels. In: Proceeding of International Seminar on Railway Axles (Edited by R. A. Smith), 2003, Imperial College London: UK.

44 Tridello A, Fiocchi J, Biffi CA, Rossetto M, Tuissi A, Paolino DS Size-effects affecting the fatigue response up to 109 cycles (VHCF) of SLM AlSi10Mg specimens produced in horizontal and vertical directions. Int J Fatigue, under review.

45 Tanaka K, Akiniwa Y. Fatigue crack propagation behaviour derived from S-N data in very high cycle regime. *Fatigue Fract Eng Mater Struct*. 2002;25: 775–784.

46 Xue H, Sun Z, Zhang X, Gao T, Li Z. Very High Cycle Fatigue of a Cast Aluminum Alloy: Size Effect and Crack Initiation. JMEPEG 2018; 27: 5406–5416.

47 Peng W, Xue H, GE R, Peng Z. The influential factors on very high cycle fatigue testing results. MATEC Web of Conferences (Fatigue 2018) 2018; 165: 20002. https://doi.org/10.1051/matecconf/201816520002

48 Zhang M. The effects of specimen size on the very high cycle fatigue properties of FV520B-I, Proceedings of the ASME 2015 Pressure Vessels and Piping Conference PVP2015 July 19-23, 2015, Boston, Massachusetts, USA

49 Mayer H. Recent developments in ultrasonic fatigue. Fatigue Fract Eng Mater Struct. 2016; 39(issue 1): 3-29.

50 Tridello A, Paolino DS, Chiandussi G, Rossetto M. Gaussian specimens for gigacycle fatigue tests: Evaluation of temperature increment. Key Eng. Mater. 2015, 625, 85–88.